

5. APR. 1983

ISSN 033

Norwegian Geophysical Society

Geophysica Norvegica

P. E. SANDHOLT
Auroral oval dynamics in relation to
solar wind-magnetosphere interaction

DET NORSKE METEOROLOGISKE INSTITUTT
BIBLIOTEKET
BLINDERN, OSLO 3

VOL. 32 NO. 4 . 1982
UNIVERSITETSFORLAGET

GEOPHYSICA NORVEGICA . VOL. 32 . NO. 4 . PAGES 77-164 . 1982

UNIVERSITETSFORLAGET

Geophysica Norvegica

is a journal of geophysics, issued under the auspices of the Norwegian Geophysical Society. *Geophysica Norvegica* is mainly intended as a journal for Norwegian authors, but papers from other authors may be accepted provided that the work has been carried out at a Norwegian institution or its content has a special relevance to Norway.

EDITOR

Jan A. Holtet, Institute of Physics, University of Oslo, P. O. Box 1048, Blindern, Oslo 3, Norway.

EDITORIAL BOARD

A. Eliassen, Institute of Geophysics, University of Oslo, P. O. Box 1022, Blindern, Oslo 3, Norway.

E. Leer, Institute of Mathematical and Physical Science, University of Tromsø, P. O. Box 953, N-9001, Tromsø, Norway.

M. Mork, Institute of Geophysics, University of Bergen, N-5014 Bergen U, Norway.

M. Sellevoll, Seismological Observatory, University of Bergen, N-5014 Bergen U, Norway.

A. Tollan, SNSF Project, P. O. Box 61, N-1432 Ås-NLH, Norway.

PUBLISHER

Universitetsforlaget: P. O. Box 2959, Tøyen, Oslo 6, Norway

P. O. Box 258, Irvington-on-Hudson, New York 10533

SUBSCRIPTION

Geophysica Norvegica is published at irregular intervals. Order from the Publisher, Universitetsforlaget.

CONTRIBUTIONS

Manuscripts conforming with the rules on page 3 of the cover should be addressed to the editor. The editorial board will appoint referees, who will ensure that the paper meets a sufficiently high scientific standard.

Auroral oval dynamics in relation to solar wind-magnetosphere interaction

P. E. SANDHOLT

Institute of Physics, University of Oslo, Blindern, Oslo, Norway

Sandholt, P. E. Auroral oval dynamics in relation to solar wind-magnetosphere interaction. *Geophysica Norwegica*, Vol. 32, No. 4, pp. 77-163, 1982.

Photometric observations of dayside auroras are compared with simultaneous measurements of geomagnetic disturbances from meridian chains of observatories on the dayside and on the nightside, to document the dynamics of dayside auroras in relation to local and global disturbances. These observations are related to measurements of the interplanetary magnetic field (IMF) from the satellites ISEE-1 and 3.

It is shown that dayside auroras shift equatorward and poleward with the growth and decay of circum-oval/polar cap geomagnetic disturbance and with negative and positive changes in the north-south component of the interplanetary magnetic field. The geomagnetic disturbance associated with auroral shift is identified as the DP2 mode. In the post-noon sector the horizontal disturbance vector of the geomagnetic field changes from southward to northward with decreasing latitude, thereby changing sign near the center of the oval precipitation region. Discrete auroral forms are observed close to or equatorward of the $\Delta H = 0$ line which separates positive and negative H-component deflections, thus in the region of sunward-convecting field lines. The reversal moves in latitude with the aurora, and it probably reflects a transition of the electric field direction at the polar cap boundary.

A model is proposed to explain the equatorward and poleward movements of the dayside oval in terms of a dayside current system which is intensified by a southward movement of the IMF vector. According to this model, the Pedersen component of the ionospheric current is connected with the magnetopause boundary layer via field-aligned current (FAC) sheets. Enhanced current intensity, corresponding to southward auroral shift, is consistent with increased energy extraction from the solar wind.

In this way the observed association of DP2 current system variations and auroral oval expansion/contraction are explained as an effect of a global, 'direct' response of the electromagnetic state of the magnetosphere due to the influence of the solar wind. The functional dependence on solar wind parameters of the transfer of electromagnetic energy to the magnetosphere is derived from a dimensional analysis. Similarly, estimates of electric field, current, and the rate of Joule heat dissipation in the polar cap ionosphere are obtained.

P. E. Sandholt, Institute of Physics, University of Oslo, P.O. Box 1048 Blindern, Oslo 3, Norway

PREFACE

The report that follows is a result of my participation in an international project to make optical observations of the polar upper atmosphere. The experimental basis for the work was provided when I took part in the data collection from the field station in

1. INTRODUCTION

The dayside aurora has received increasing attention during the last decade. This is primarily due to its association with the cusp in the magnetic field configuration of the magnetosphere. The location, extent, dynamics, and energy distribution of magnetosheath particles entering the upper atmosphere along the magnetospheric cusp can be determined by monitoring the optical signatures of the interaction between these particles and atmospheric constituents. The same optical emissions also yield information on the F-region dynamics and the characteristics of atmospheric species.

Studies of the cusp region relate to fundamental questions concerning the interaction between the solar wind and the magnetosphere. Some important topics are: Effects of the interplanetary magnetic field (IMF) on the topology and stability of magnetospheric boundary layers and the mechanisms of transfer of plasma and electromagnetic energy from the solar wind to the magnetosphere. Furthermore, how much of the energy released during magnetospheric substorms comes from energy previously stored in the magnetotail and how much is directly extracted from the solar wind? Related to the above questions is the response of the dayside aurora to magnetospheric substorms and to IMF variations. In this report primary attention is focused on latitudinal shifts of the dayside aurora in relation to substorm perturbations and IMF variations.

The experimental part of the report is based on photometric observations of dayside auroras from Svalbard, Norway. These observations are compared with simultaneous measurements of geomagnetic disturbances, to document the auroral dynamics in relation to local and global dis-

turbances. This is based on a close examination of geomagnetic records from meridian chains of observatories on the dayside and on the nightside. The auroral and geomagnetic variations are related to measurements of the interplanetary magnetic field from the satellites ISEE-1 and 3.

Equatorward movements of the dayside aurora can be regarded as indicating a transfer of geomagnetic flux from the dayside to the nightside. Customarily, this erosion of the dayside magnetosphere is seen as a consequence of increased merging of interplanetary and magnetospheric field lines. The dual description is in terms of day and nightside current systems that are partly on the magnetopause and in part internal to the magnetosphere. An alternative interpretation of the shift of the dayside aurora is in terms of a reconfiguration of the magnetotail current circuit associated with magnetospheric substorms (cf. Eather et al. 1979). According to this model the substorm is a driven process, resulting directly from an enhanced efficiency of the solar wind-magnetosphere dynamo. This theory is at variance with the widely accepted substorm picture that describes the mechanism as an unloading process, whereby excess magnetic field energy that has accumulated in the magnetotail is rapidly released, with some of the energy transferred to particle kinetic energy (i.e. the 'growth phase' model). The understanding of details of the time-sequence and phenomenology of the magnetospheric substorm is still one of the most important and urgent tasks of magnetospheric physics (Roederer, 1977). Only data from a worldwide network of geophysical observatories and onboard the satellites can provide a consideration of the substorm as a global phenomenon. This is one of the main objectives of the extended geophysical investigations during the period of Interna-

tional Magnetospheric Study (Roederer, 1977).

It has been questioned whether it is possible to determine the separate roles played by IMF variations and substorms as they cannot be regarded as independent phenomena. Nevertheless, there have been claims of separating the dependence of cusp and dayside aurora location on IMF and substorm perturbations. Burch (1973) found that he could predict the latitude of the poleward and equatorward sides of the cusp with rms errors of 1.34° and 1.16° , respectively from a knowledge of the average Z-component of IMF for the previous 45 min., independent of the substorm activity. Eather et al. (1979) claimed to show that the equatorward motion of midday auroras is directly connected with substorm activity and not with the north-south component of the IMF. They specifically noted that a southward turning of the IMF, without concurrent substorm activity, does not cause equatorward motion of the dayside aurora.

A synthesis between these two opposite positions is represented by Kamide et al. (1976). They concluded, on the basis of a statistical study of polar satellite data, that both IMF and substorms have about the same amount of influence in terms of the latitudinal shift of the dayside aurora.

For the purpose of separating the IMF and substorm effects on the dayside aurora we try to separate the directly IMF related and the substorm related components of geomagnetic disturbances. In order to do this, simultaneous observations from different meridian chains of observatories are necessary. Special attention is placed on the local geomagnetic disturbances observed to be associated with latitudinal movements of the dayside aurora. As far as the author knows, the temporal and spatial relationships between dayside auroral dynamics and day-

side geomagnetic disturbances are not documented in earlier studies.

Observations by satellite-borne magnetometers (Sugiura and Potemra 1976; Iijima and Potemra 1976a, b) showed the overall field-aligned current system of the cusp region. From combined satellite- and ground-based observations Wilhelm et al. (1978) investigated the relationship between ionospheric and field-aligned currents in the dayside cusp.

Studies of dayside currents including satellite-data on convection electric fields and energetic particles are reported by Saflekos et al. (1979) and Bythrow et al. (1981). Thus, measurements from polar orbiting spacecrafts have provided valuable information on the gross features of electric fields and currents in and above the dayside polar ionosphere. However, the spatial extent, the dynamics, and the relationship to the dayside aurora are not well known.

As this study is part of a multinational project for optical observations of the dayside cusp atmosphere, the presentation starts with a brief overview of the observation program and the experimental techniques which are used (Chapter 2).

As a background for the presentation of the experimental data in Chapter 4, theoretical and experimental information on the more general aspects of the electrodynamic of solar wind-magnetosphere interactions are given in Chapter 3. Chapter 5 contains a review of later work with special relevance to the discussion of the experimental data in Chapter 6. Summary and conclusions are found in Chapter 7.

2. THE OBSERVATION PROGRAM AND EXPERIMENTAL TECHNIQUES

2.1 Introduction

Owing to the inaccessibility of suitable

ground observatories, the morphology of the dayside aurora has been documented almost exclusively by satellite and aircraft measurements. Optical observations of midday auroras from the ground set requirements both to the geographic latitude to avoid scattered sunlight and to the geomagnetic latitude to be under the dayside auroral oval. The only accessible stations in the northern hemisphere which satisfy these requirements

are seen in Fig. 2.1 to be on Svalbard, at the edge of the polar sea north of Norway (near latitude 79° N, longitude 15° E).

During the winter of 1978–79 a multinational, cooperative project for optical observations of the dayside upper atmosphere was undertaken at Svalbard. The observation-program/technics were up-dated during the following three winters. Researchers from the Universities of Tromsø and Oslo (Nor-

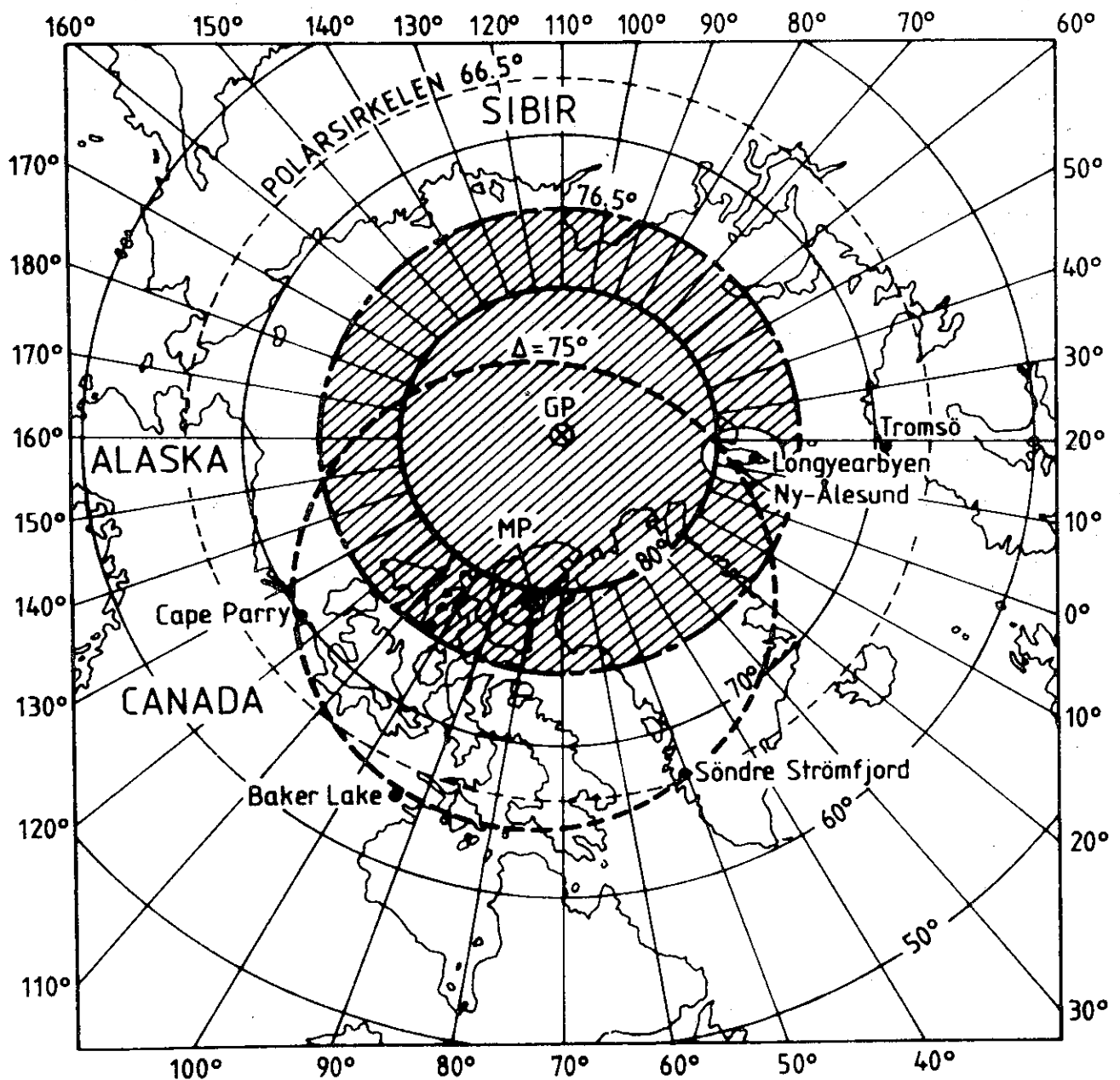


Fig. 2.1. Map showing the northern polar cap where the sun is more than 10° below horizon during midwinter (shaded). The 75° invariant latitude circle indicates the typical location of the midday aurora.

way), the University of Alaska (United States), Ulster Polytechnic and the University of Southampton (United Kingdom), and the University of Saskatchewan (Canada) participated in this project.

The observatory buildings and larger pieces of equipment were assembled in Longyearbyen, on the island group West Spitsbergen. The major instruments deployed for the program are listed in Table 2.1. A short description of four major objectives of the project and the related experimental techniques are given in the following subsections. The finer spectroscopy of dayside emissions

(Sect. 2.4) and F-region neutral winds (Sect. 2.5) will not be further discussed in this report. For more information on these subjects, cf. Deehr et al. (1980), Sivjee et al. (1982), and Smith and Sweeney (1980).

2.2 Latitude and local time variations of day-side auroral emissions

The location, altitude and brightness of day-side auroral forms as function of time were monitored by using two sets of multichannel meridian-scanning photometers (MSP), one at Longyearbyen and the other at Ny Ålesund. Longyearbyen and Ny Ålesund are

TABLE 2.1

Instrument Type, Deployment, and Purpose for the Svalbard Expedition 1978-1979

Instrument	Institution	Location	Purpose
All-sky camera (35 mm, black and white)	GI	LYR	Location and orientation of auroral arcs and bands.
All-sky camera (16 mm, color)	UT	NYA	
Meridian-scanning photometer	GI	LYR	Mapping of local time position of red (6300 Å) cusp and discrete bands and associated characteristic energy of precipitating particles.
Meridian-scanning photometer	US	LYR	
Meridian-scanning photometer	NIKF	NYA	
Meridian-scanning photometer	GI	PKR, FYU	
Zenith LLLTV	NIKF	LYR	Morphology of fast-moving bands
Fabry-Perot interferometer (6300 Å)	UP	LYR	Doppler wind and temperature of neutral F region.
1-m spectrophotometer (3000-8700 Å)	GI	LYR	Spectroscopic studies of various atmospheric emissions.
½-m spectrophotometer	GI	LYR	
Magnetometer	UT	NYA	Determination of substorm-related effects.
Magnetometer	UT	BJØ	
Magnetometer	UT	TOS	
Magnetometer chain (seven instruments in Alaskan Chain)	GI	AK	

	Symbol
Geophysical Institute	GI
Norwegian Institute of Cosmic Physics	NIKF
Ulster Polytechnic	UP
University Saskatchewan	US
University of Tromsø	UT
Ny Ålesund	NYA
Longyearbyen	LYR
Bjørnøya	BJØ
Tromsø	TOS
Alaskan Chain	AK
Poker Flat	PKR
Fort Yukon	FYU

All meridian-scanning photometers include 4278-Å N_2^+ , 6300-Å O I, 5577-Å O I, and 4861-Å H beta.

located approximately along the same meridian with a separation of 117 km (cf. Table 4.3). The Ny Ålesund equipment consisted of a six-channel, rotating-filter-wheel photometer with a single photomultiplier while the former had four independent photometers. Both systems employed a single rotating mirror and a 1° field of view for each channel. The photometers were equipped with $\sim 20 \text{ \AA}$ filters. The complete magnetic meridian scan took about 20 s. The photometer system at Longyearbyen was coupled to a real-time digital data handling system consisting of a 64 k byte mini-computer, a 9-track, digital magnetic tape recorder-reproducer, an interactive graphics unit and an electrostatic copier.

One example of typical noon-time single-photometer scans obtained simultaneously from Longyearbyen and Ny Ålesund, on Dec. 19, 1979, is shown in Fig. 2.2. No corrections have been applied to these data. Peak intensities above background are given on the Longyearbyen traces. This type of data will be presented and analysed in Chapters 4 and 6.

The MSP systems were placed at both stations for the purpose of extending the latitude coverage and to determine the spatial extent of auroral emissions by triangulation.

An example illustrating the triangulation technic used to estimate the altitude and latitude position of luminosity is shown in Fig. 2.2b. Assuming that the auroral form is aligned along the magnetic field (indicated by the dashed line in the Figure), the zenith angles at which the emission reaches maximum intensity, half max. intensity, and background level were used to draw parallelogram boundaries for the cross-section of the auroral arc. This is considered a first approximation to the spatial extent of light emission.

It is known that the luminosity across the width of the arc increases gradually from the edges to the center (cf. Romick and Belon 1967a, b). In order to determine the profile of the volume emission rate within the arc, a more refined analysis is needed. The procedure used by Romick and Belon was as follows: Starting with approximate assumptions of horizontal (H) and vertical (V) distributions of luminosity (trial functions) the functional form of the volume emission $\rho(h, \lambda)$ was obtained. From $\rho(h, \lambda)$ intensity versus zenith angle curves for both stations could be generated. Then the various parameters in the H and V functions were adjusted until agreement with the observed data was reached at both stations.

The latitude position of auroral forms is a key parameter for the main discussion of this report. To obtain that information, the graphical technic shown in Fig. 2.2b was used. When information from both stations was not available, maximum emissions heights were estimated from absolute intensities and intensity ratios of auroral emissions (cf. Rees and Luckey 1974).

2.3 Dayside emissions in relation to substorm perturbations and interplanetary magnetic field

The prime objective of this part of the observation program and of this report is to document the nature of the response of dayside emissions to substorm perturbations and to changes in the interplanetary magnetic field (IMF).

The study is based on photometric observations of auroras in the midday and post-noon sectors of the auroral oval from the two stations on Svalbard. The observed emission height and zenith angle were used to calculate the geographical position of the dayside aurora in the meridian as a function of local time (cf. Sect. 2.2). By this method

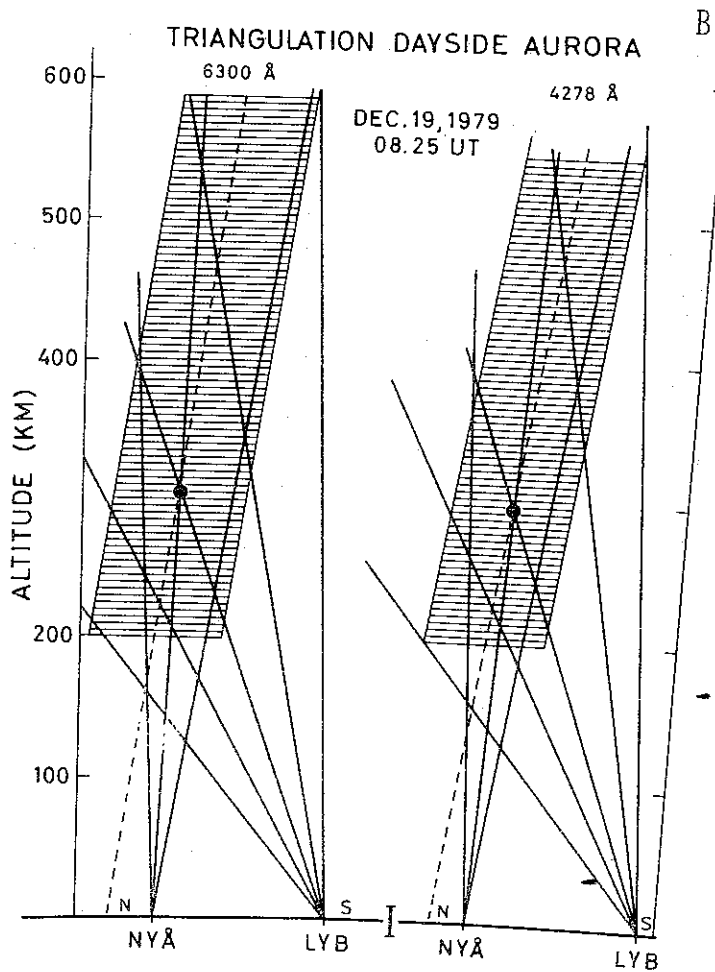
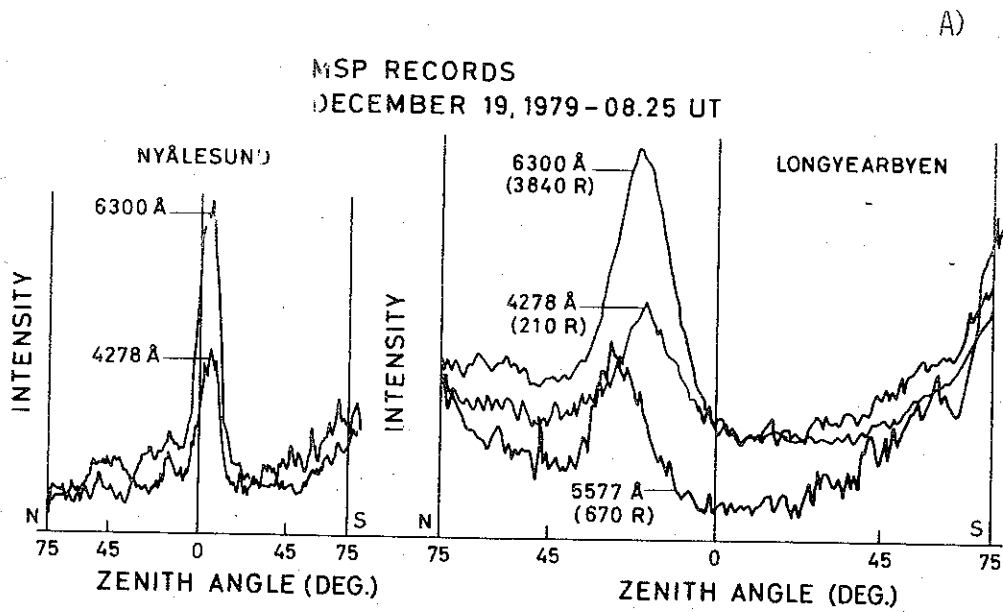


Fig. 2.2. (a) Two station meridian scanning photometer records of a typical midday auroral arc. (b) Showing the graphical technic used in estimating parallelogram boundaries of auroral luminosity from the traces in Fig. A).

the location of the aurora can be determined within the range $\sim 69\text{--}80^\circ$ geomagnetic latitude (cf. Fig. 4.18). During midwinter sunlight is no problem.

Local magnetic activity was monitored at six stations along the Norway–Kola meridian chain covering the range of geomagnetic latitude $62.8\text{--}75.4^\circ$ (from Apatity to Ny Ålesund).

Along this chain of observatories local magnetic noon corresponds to ~ 09 UT. Observations of simultaneous nightside activity were obtained from the Alaska IMS chain of stations as well as a net of observatories in Canada operated by University of Alberta. Together the Alaskan/Canadian and Norway/Kola observatories constitute a transpolar net of stations which is well suited as a basis for study of day-nightside relationships in magnetic/auroral behavior. The simultaneous evening sector of the auroral oval is covered by the Russian arctic stations Dixon Island and Tixie Bay. The location of the geomagnetic observatories used is shown in Fig. 2.3.

Professor Leiv Harang based his pioneering work on polar geomagnetic storms on observations from a Scandinavian net of observatories. But he was aware of the limitations of this data base. As Harang (1946) states:

'For a closer examination along the entire auroral zone, especially of the discontinuities and the "positive" and "negative" sections, the material is not sufficient. In order to solve this question one ought to have a similar dense net of recording stations along a meridian lying on the American side of the polar region, say along geomagnetic longitude 260° , similar to the line from Spitzbergen over Bear Island and the Scandinavian peninsula.' Thus, for a close investigation of substorm behavior, separating space and time variations, simultaneous observations

from different meridian chains are necessary.

Information on the interplanetary magnetic field was obtained from the two satellites ISEE (International Sun-Earth Explorer) 1 and 3. ISEE-3 was launched into a halo orbit about the libration point more than 200 earth radii upstream of the earth. The orbit of ISEE-1 had an apogee of 23 earth radii and a perigee of 280 km with a period of ~ 58 hours.

2.4 Spectrophotometric observations

To reveal the finer details of the spectrum of atmospheric emissions associated with dayside auroras, two Ebert-Fastie spectrophotometers were operated from Longyearbyen. One of the spectrometers has a focal length of 1 meter and employs a $25.6 \times 15.4 \text{ cm}^2$ grating and 15 cm long curved slits. The second spectrometer has a focal length of $\frac{1}{2}$ meter and is fitted with a $12 \times 7 \text{ cm}^2$ grating and curved slits, each 7 cm long. Both spectrometers are mounted in an insulated spherical shell and aligned to view the same region of the sky. Remotely controlled elevation-azimuth drive of the housing facilitates the pointing of the spectrometers in any desired direction. Spectroscopic measurements are made in the second or third order using broad-band, glass filters to isolate the desired wavelength region. Examples of ultraviolet spectrograms from the 1 meter spectrometer which was pointing into different auroral forms near zenith in the noon and post-noon sectors, respectively, are shown in Fig. 2.4.

2.5 Neutral F-region winds from optical interferometric observations of the 6300 \AA OI emission

High-resolution interferometric measurements of the OI 6300 \AA line were made with a Fabry-Perot interferometer using 127-mm

GEOMAGNETIC H-COMPONENT RECORDS/DAYSIDE AURORAL LOCATION
 JAN. 15, 1979

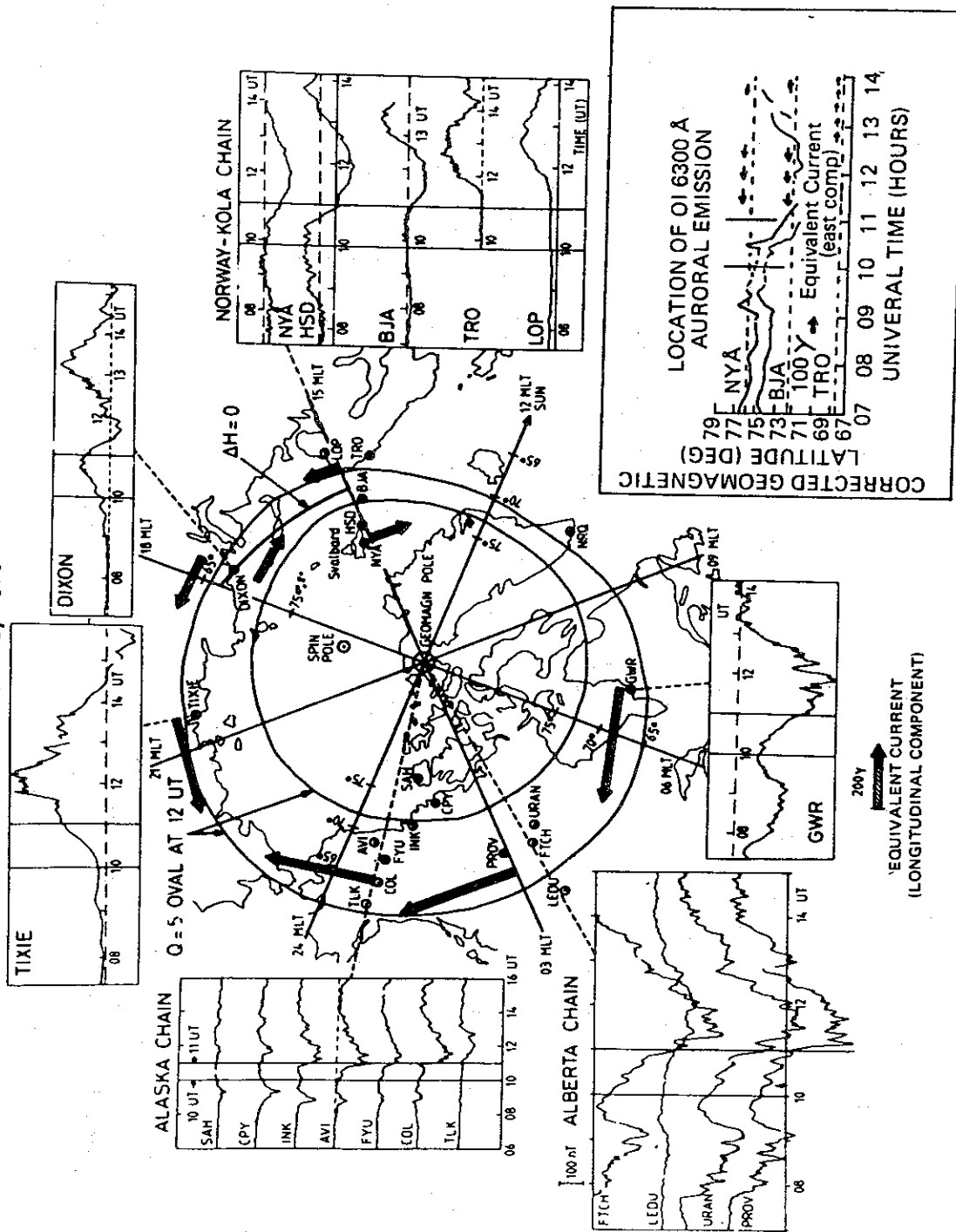


Fig. 2.3. Showing the location of geomagnetic observatories with corresponding magnetometer traces. The instantaneous position in magnetic local time of the Norway-Kola chain, the Alaska chain and some Canadian stations are given for 12 UT. The location of post-noon sector aurora is shown in the lower right panel.

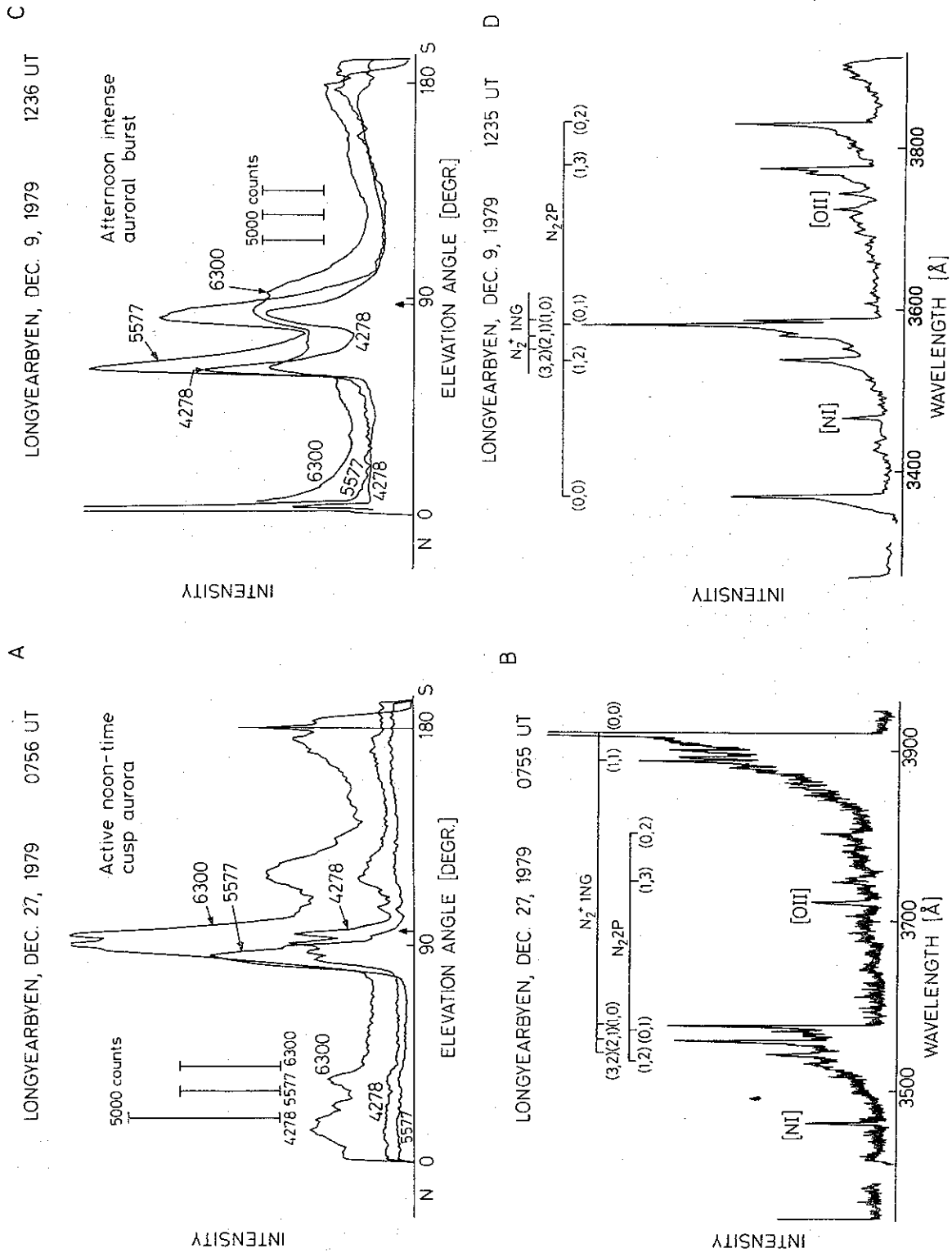


Fig. 2.4. Meridian scanning photometer and spectrometer records obtained at Longyearbyen, Svalbard. Photometer calibration factors are: 4278 Å-0.3 R/C; 5577 Å-0.9 R/C, and 6300 Å-0.93 R/C. The arrow on the abscissa axes marks the elevation angle of the spectrometer obtaining the simultaneous spectrum. Panels A and C: MSP records of active midday cusp and post-noon sector intensification of the aurora, respectively. Panels B and D: Near ultraviolet spectrograms of the two auroras shown in A and C.

diameter plates spaced 8, 9 mm apart and modulated piezoelectrically. The long-term stability of this instrument was such that it was possible to make relative measurements of wavelength to a precision of $4 \times 10^{-4} \text{ \AA}$ with a typical integration time of 6–12 minutes. The instrument was used to measure the Doppler-shift of the 6300 \AA line in the auroral spectrum and hence to obtain determinations of the neutral air velocity at the height of emission, to find its diurnal variation and its response to individual auroral events (cf. Fig. 2.5). A continuous record of winds to be used in the study of neutral atmospheric dynamics was obtained (cf. Smith and Sweeney 1980).

JAN. 27th, 1979

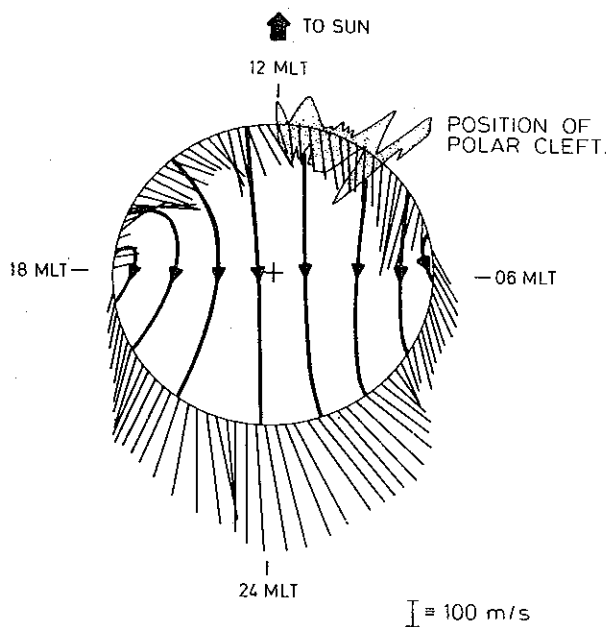


Fig. 2.5. A 24 h plot of the thermospheric wind for 27 January 1979 drawn with the geomagnetic pole at the center and the path of the observing site shown as a circle. The wind vector interpolated measurements are shown in azimuth and magnitude by light lines. The thick black lines show the kind of wind pattern which is consistent with these measurements. Magnetic local time, used in this figure, is 3 h ahead of universal time (Smith and Sweeney 1980).

3. ELECTRODYNAMICS OF SOLAR WIND-MAGNETOSPHERE INTERACTIONS

3.1 Introduction

The description of solar wind-magnetosphere interactions can be grouped into essentially different approaches. One approach is based on the magnetic flux tube description, another on the electric current description. Dungey (1961) and others describe the interaction in terms of a cutting and 're' connection of geomagnetic field lines when they make contact with the interplanetary magnetic field. According to Alfvén (1977) the coupling between the solar wind and the magnetosphere is mediated by current systems on the interface between the two media, the magnetopause. A third approach was put forward by Axford and Hines (1961). The energy transfer to the magnetosphere was explained by viscous interactions along the magnetopause.

In Sect. 3.2. the solar wind-magnetosphere energy coupling is illustrated by the application of Poynting's theorem to an idealised, open model of the magnetosphere. The functional dependence of the energy transfer on solar wind parameters is derived on the basis of a dimensional analysis. Implications of the reconnection hypothesis are discussed. Viscous- and diffusion models of the low-latitude magnetopause boundary layer are reported in Sect. 3.3. Sect. 3.4 is a review of the main features of the magnetospheric substorm.

3.2 The open magnetosphere

3.2.1 The solar wind-magnetosphere dynamo

When geomagnetic field (GMF) lines, emanating from the earth's polar cap, are directly inter-connected with interplanetary field (IMF) lines, the magnetosphere is said to be 'open'. Interconnected field lines will give the solar wind an easy means to transfer flow

momentum to the magnetospheric plasma.

The solar wind exerts a magnetic shear stress on the lateral surface of the magnetotail. The work done by this surface stress constitutes an energy input to the magnetosphere. The interaction along the magnetopause is a dynamo process which converts kinetic energy from the solar wind to electrical energy which is dissipated inside the magnetosphere. This energy transfer to the magnetosphere can be expressed by the application of Poynting's theorem.

The conservation of energy within a finite volume V of a medium with current density \vec{j} and electromagnetic fields \vec{E} and \vec{B} reads:

$$\int_V -\nabla \cdot \vec{S} d^3x = \int_V \left[\vec{j} \cdot \vec{E} + \frac{\delta}{\delta t} \times \left(\frac{B^2}{2\mu_0} + \frac{1}{2}\epsilon_0 E^2 \right) \right] d^3x \quad (3.1)$$

where $\vec{S} = \mu_0^{-1} \vec{E} \times \vec{B}$ is the Poynting vector. The energy influx through the surface of the volume equals the time rate of change of electromagnetic energy plus the total work done by the \vec{E} -field on the sources within the volume (cf. Jackson 1962 p. 190).

An idealized model of the magnetospheric tail is a cylinder with length L_T and radius R_T as is shown in Fig. 3.1. Applied to this geometry Eq. 3.1 is reduced to:

$$\begin{aligned} \iint_A \vec{S} \cdot \vec{n} da &= 2\mu_0^{-1} L_T \int_{abc} \vec{E} \times \vec{B}_T dl \\ &= L_T \int_P \int_S (\vec{j} \cdot \vec{E}) dy dz + 2L_T \iint_{abcd} \frac{\delta}{\delta t} \\ &\quad \times \left(\frac{B_T^2}{2\mu_0} \right) dy dz, \end{aligned} \quad (3.2)$$

where A represents the surface area of the magnetotail of the length L_T , \vec{n} is a unit

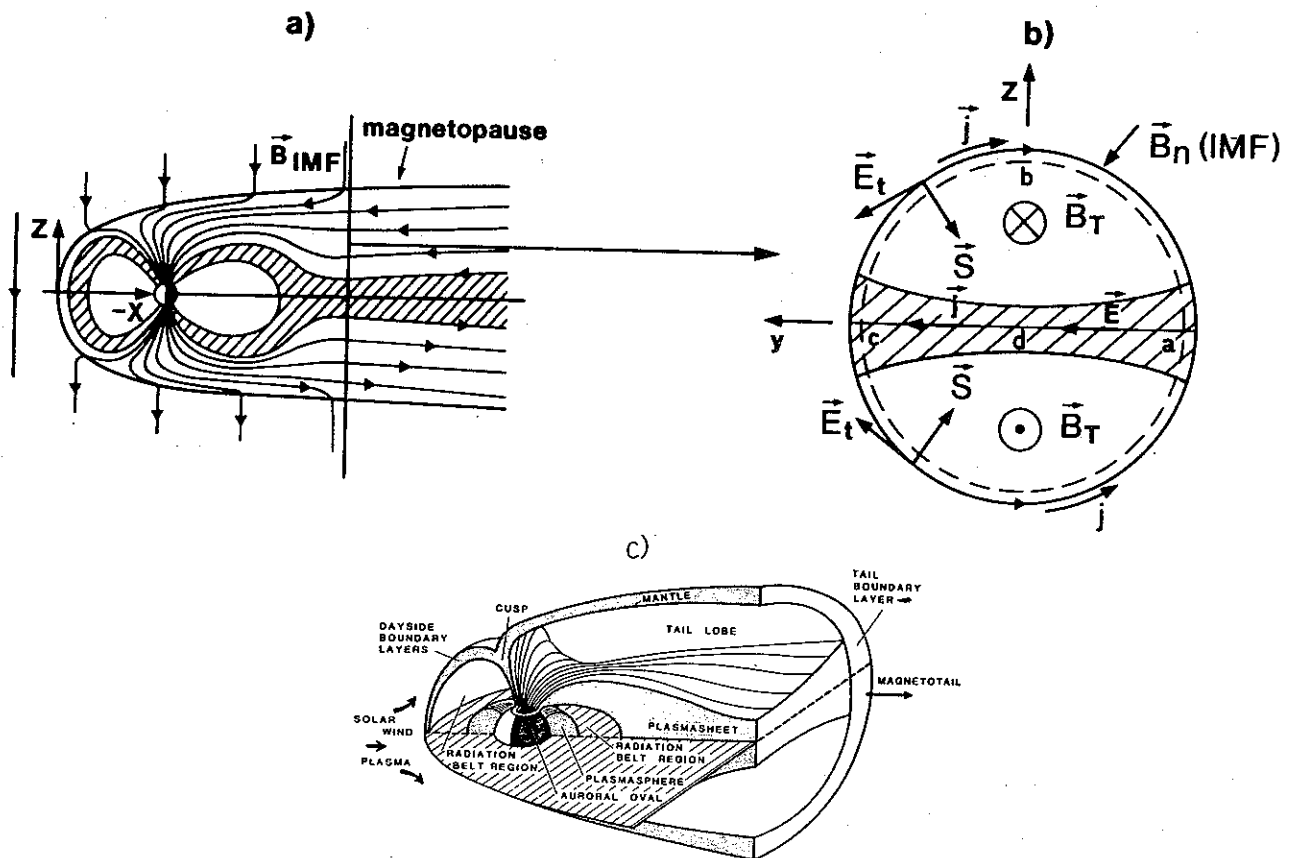


Fig. 3.1. (a) A sketch of magnetotail topology. (b) A cross-section of the magnetotail showing the current system and the geometry used in the Poynting theorem analyses. (c) Showing the principal magnetospheric plasma regions and how they are connected via magnetic field lines with the upper atmosphere.

vector normal to the magnetopause and B_T is the magnetotail field. The electromagnetic energy transferred to the magnetosphere is converted to magnetic field energy and/or dissipated as particle heating and fluid acceleration within the plasma sheet (PS).

Faraday's law of electromagnetic induction applied to our system, is expressed by

$$\int_{abc} \mathbf{E}_t \cdot d\mathbf{l} = \int_{adc} E_y^{PS} dy - \iint_{abcd} \frac{\delta \vec{B}_t}{\delta t} \cdot \vec{n} da \quad (3.3)$$

During steady state conditions (no macroscopic changes of the magnetic field) the energy transfer to the magnetosphere is expressed by

$$Q = 2\mu_0^{-1} L_T B_T \phi_{CT};$$

$$\phi_{CT} = \int_{abc} \mathbf{E}_t \cdot d\mathbf{l} = \int_{adc} E_{PS} dy \quad (3.4)$$

In the absence of magnetic energy changes the energy influx can be totally dissipated in the plasmasheet. The dissipation rate is controlled by the induced potential difference ϕ_{CT} across the magnetotail which is determined by the solar wind parameters u_I and B_I (see Fig. 3.1):

$$\phi_{CT} = - \int_{abc} \vec{u}_I \times \vec{B}_n \cdot d\mathbf{l} = u_I \int_{abc} B_n dl$$

$$= u_I \vec{B}_n \cdot \pi R_T \quad (3.5)$$

and

$$Q = I_T \phi_{CT}; I_T = 2\mu_0^{-1} B_T L_T \quad (3.6)/(3.7)$$

where I_T is the magnetotail dynamo current induced on the magnetopause by a polarization of the solar wind driven by the Lorentz force $q\vec{u}_I \times \vec{B}_I$.

The amount of open flux emanating from the earth's polar cap is expressed by the

magnetotail parameters R_T and B_T ,

$$\psi = \frac{1}{2} \pi R_T^2 \cdot B_T \quad (3.8)$$

B_T is assumed to be rather homogeneous across the tail.

Combining Eqs (3.7) and (3.8) we have the following relationship between the magnetotail dynamo current I_T and the amount of open geomagnetic flux ψ :

$$I_T = \mu_0^{-1} \frac{4L_T}{\pi R_T^2} \cdot \psi \quad (3.9)$$

We notice the direct proportionality between I_T and ψ at the time of a steady state magnetic field configuration in the magnetosphere.

Intending to express the power input to the magnetosphere (Q) in terms of solar wind parameters u_I and B_I , we use the following Eqs:

$$u_I \vec{B}_n \cdot \pi R_T (= \phi_{CT})$$

$$= l_R u_I B_I \sin^2 \frac{\theta}{2} (= \phi_{PC}) \quad (3.10)$$

$$\frac{1}{2} \pi R_T^2 B_T = \pi R_T L_T \vec{B}_n \quad (3.11)$$

where ϕ_{pc} is the polar cap potential drop and θ is the polar angle of the component of the interplanetary field perpendicular to the sun-earth line measured from the northward geomagnetic axis (cf. Eq. 3.22 and Fig. 3.6) and l_R is the length of the reconnection line on the frontside magnetopause (cf. Sect. 3.2.2.).

Equation 3.10 relates the tangential electric field as being mapped from the voltage across the polar cap ($\phi_{CT} = \phi_{pc}$). Equation 3.11 expresses the conservation of open flux as it is swept from the polar cap into a tail lobe and eventually goes across the magnetopause in receding to the interplanetary space (Yeh et al. 1981). From Eqs 3.5, 3.6,

3.10, 3.11 we have:

$$Q = \frac{4}{\mu_0} \frac{L_T^2}{\pi R_T^2} u_I B_I^2 \sin^4 \frac{\theta}{2} l_0^2 \quad (3.12)$$

expressed in watts. According to Perrault and Akasofu (1978) an empirical expression for the total energy coupling between the solar wind and the magnetosphere is:

$$\varepsilon(t) = \frac{4\pi}{\mu_0} u_I B_I^2 \sin^4 \frac{\theta}{2} l_0^2, \quad (3.13)$$

where l_0 is a length parameter which is related to the size of the magnetosphere and set equal to $7R_E$. $\varepsilon(t)$ has the physical unit of watts. We note that the expression for the energy transfer given in Eq. 3.12 corresponds to the empirical relation 3.13 if l_0 can be expressed by

$$l_0 = \frac{L_T}{\pi R_T} \cdot l_R \quad (3.14)$$

Here L_T is the effective length of the tail current sheet.

The solar wind values $u_I = 500$ km/s, $B_I = 5$ nT and $\theta = 180^\circ$ (southward directed IMF) give for the total power of the solar wind-magnetosphere dynamo:

$$\varepsilon = 2.5 \times 10^{11} \text{ W.}$$

This is $\sim 0.01\%$ of the energy flux in the solar plasma flow over the cross-sectional area of the magnetosphere in a plane perpendicular to the sun-earth line.

In analogy to (3.1) the conservation of linear momentum within the volume reads (cf. Jackson 1962 p. 193):

$$\begin{aligned} \frac{d}{dt} (P_{\text{mech}} + P_{\text{field}}) &= \int_V (\rho \vec{E} + \vec{j} \times \vec{B}) \\ &\times d^3x + \varepsilon_0 \frac{d}{dt} \int_V \vec{E} \times \vec{B} d^3x \\ &= \iint \vec{n} \cdot \vec{T} da, \end{aligned} \quad (3.15)$$

where $\varepsilon_0 \vec{E} \times \vec{B}$ is the linear momentum of the electromagnetic field and \vec{T} is the Max-

well's stress tensor. The elements of the tensor are

$$T_{ij} = \mu_0^{-1} [E_i E_j + B_i B_j - \frac{1}{2} \delta_{ij} (E^2 + B^2)]$$

The product $\vec{n} \cdot \vec{T}$ in (3.15) represents the normal flow of momentum per unit area into the volume V through the surface A . Applied to our system $\vec{n} \cdot \vec{T}$ is the force per unit area transmitted across the surface A of the magnetotail, i.e. the magnetopause. It can be shown that

$$\vec{n} \cdot \vec{T} da \cong \mu_0^{-1} B_t B_n \cdot A \quad (3.16)$$

where B_t and B_n are the tangential and normal components of the magnetic field on the magnetopause. Equation (3.16) expresses the transfer of flow momentum of the solar wind to the magnetospheric plasma by magnetic shear stresses exerted on the magnetotail surface.

For a recent theoretical discussion of the solar wind-magnetosphere energy transfer, considering the magnetopause as a rotational discontinuity ($B_n \neq 0$), cf. Lee and Roederer (1982).

3.2.2 Reconnection at the dayside magnetopause

Reconnection in the sub-solar region. In the following we will describe the coupling between the interplanetary medium and the magnetosphere in terms of reconnection models, applied to the dayside magnetopause.

When they make contact with interplanetary field lines on the dayside magnetopause geomagnetic field lines (having both feet on the earth) are cut and 're' connected. The locus of points where the reconnection occurs are considered to form a line, called the reconnection line (cf. Figs 3.2 and 3.3).

The interplanetary electric field ($\vec{E}_I = -\vec{u}_I \times \vec{B}_I$) can penetrate into the magnetosphere via connected field lines. The potential

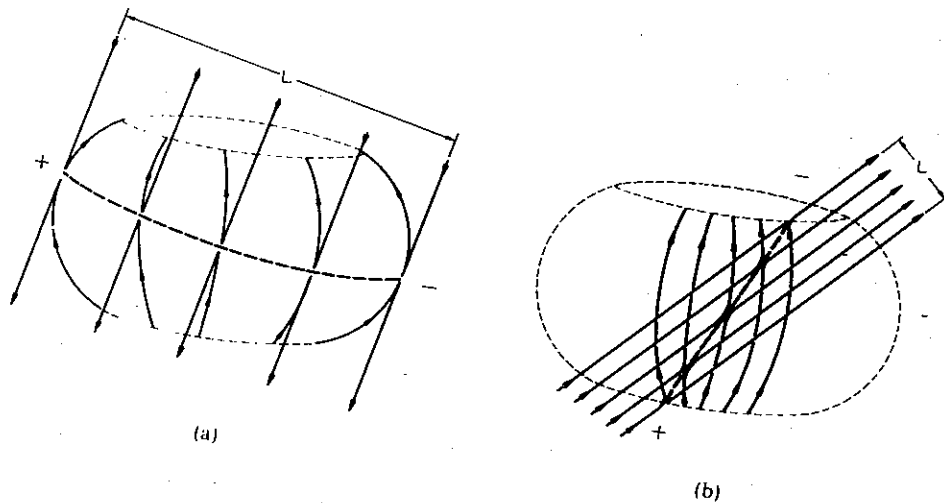


Fig. 3.2. Schematic drawing illustrating the reconnection line (---) passing the nose of the magnetopause. IMF is supposed to be oriented south-west in (a) and north-east in (b). The polarity of the electric field is indicated by + and - signs (Nishida and Maezawa 1971).

difference thus introduced into the magnetosphere is proportional to the lateral width (L) of the reconnecting IMF field lines, and it will vanish if the reconnection line is reduced to a point.

The magnetic fields on interplanetary and geomagnetic sides of the magnetopause are denoted by \vec{B}_1 and \vec{B}_2 . If the ratio B_1/B_2 and the angle α between \vec{B}_1 and \vec{B}_2 do not vary much on the entire magnetopause, the electric potential drop along the reconnection

line is estimated by

$$\begin{aligned} \phi &= E_1 \sin(\alpha - \beta) l_R \\ &= u_1 B_1 l_R F_1 \left(\frac{B_1}{B_2}, \alpha \right) \end{aligned} \quad (3.17)$$

or equivalently

$$\phi = E_2 \sin \beta l_R = u_2 B_2 l_R F_2 \left(\frac{B_1}{B_2}, \alpha \right) \quad (3.18)$$

where l_R is the length of the reconnection line and β is the angle characterizing the

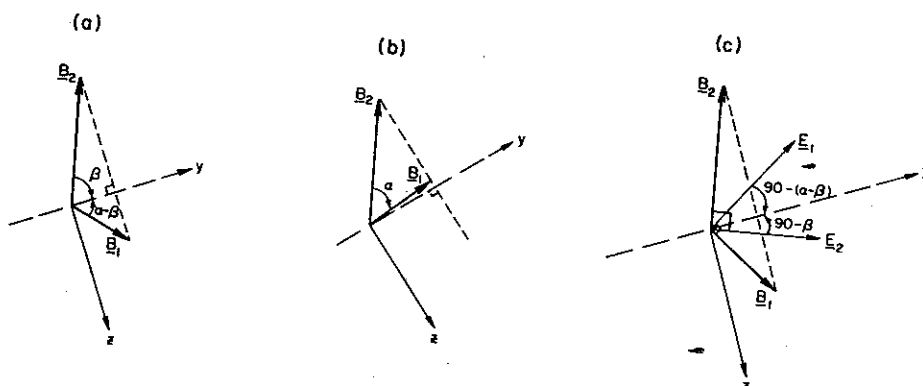


Fig. 3.3. The orientation of the reconnection lines with respect to magnetic fields (\vec{B}_1 and \vec{B}_2) and electric fields (\vec{E}_1 and \vec{E}_2). Subscript 1 and 2 refer to different sides of the interface. The reconnection occurs in (a) but not in (b), and (c) illustrates the electric fields for (a) (Gonzales and Mozer 1974).

local direction of the reconnection line relative to the local GMF B_2 (cf. Nishida 1978 p. 69).

Making the required corrections to Eqs (3.17) and (3.18) by taking into account the spatial variations of \vec{B}_1 and \vec{B}_2 , Gonzales and Mozer (1974) derived the following expression:

$$\phi = \frac{2u_I B_{I,t} R F_1 \left(\frac{K B_{I,t}}{B_G}, \alpha_0 \right)}{\sin(\alpha_0/2)} \quad (3.19)$$

where $B_{I,t}$ is the tangential component of the IMF, R is the radius of the dayside magnetopause, $K B_{I,t}/B_G$ is the ratio of interplanetary and geomagnetic fields at the nose of the magnetopause (K being the amplification factor of the field at the bow shock), and α_0 is the value of the α angle at the nose of the magnetopause.

Figure 3.4 is a comparison of the electric field calculated from formula (3.19) with that observed in the polar cap. The measured field is the dawn-dusk component of the electric field observed by balloons at the polar cap stations Resolute Bay and Thule. The calculation of ϕ is made by using the following parameters and simultaneous IMF

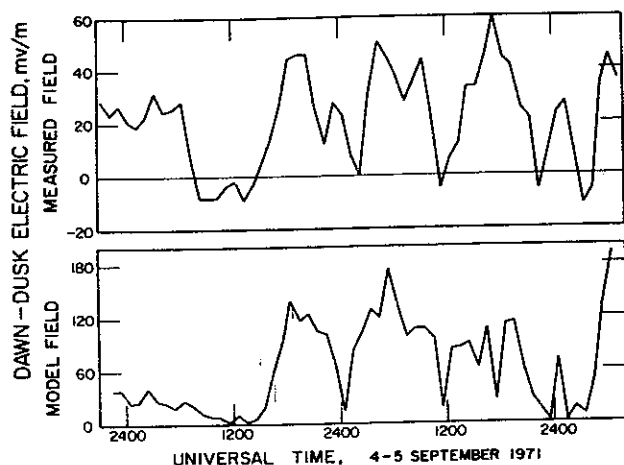


Fig. 3.4. Comparison of electric fields measured by balloons in the polar cap (top) and calculated (see text) (Gonzales and Mozer 1974).

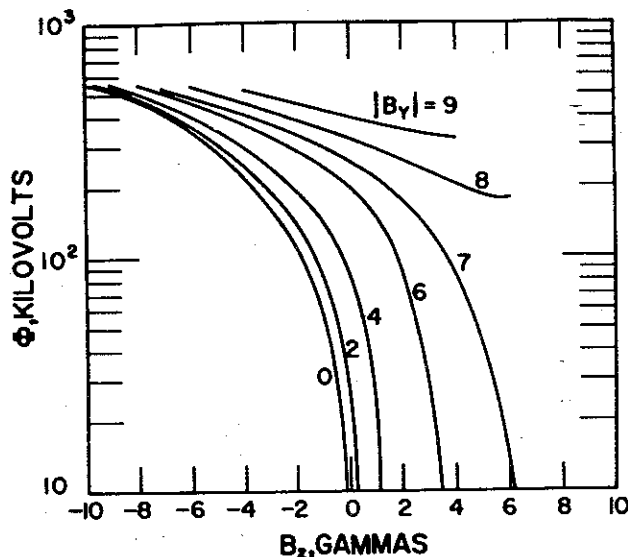


Fig. 3.5. A model calculation of electric potential difference produced along the reconnection-line. B_y and B_z are components of IMF (Gonzales and Mozer 1974).

observations: $B_G = 70 \gamma$, $R = 15 R_E$, $K = 5$, $u_I = 300 \text{ km/s}$ and the diameter of the polar cap is estimated to be 3000 km.

The factor $\sim 1/3$ between the measured E-field and the model field is interpreted to represent the fraction of the interplanetary field lines that can reach the reconnection line. Only $1/3$ can make it, the remaining are deflected and pushed aside to the flanks of the magnetosphere without even touching the reconnection line.

Equation (3.19) can be rewritten in terms of the components of B_I :

$$\phi = \frac{2^{3/2} u_I B_{I,t}^{\frac{1}{2}} R (K B_{I,t}^2 - B_G B_{I,z})}{(B_{I,t} - B_{I,z})^{\frac{1}{2}} \times (K^2 B_{I,t}^2 + B_G^2 - 2K B_G B_{I,z})^{\frac{1}{2}}} \quad (3.20)$$

where $B_{I,t} = (B_{I,y}^2 + B_{I,z}^2)^{\frac{1}{2}}$ and $B_{I,t} \cos \alpha_0 = B_{I,z}$. ϕ is plotted in Fig. 3.5 versus $B_z (= B_{I,z})$ using $B_y (= B_{I,y})$ as a parameter. From Fig. 3.5 it seems possible that the observed correlations between southward B_z and the DP2 mode of geomagnetic activity (cf. Sect. 5.2) are reflections of the IMF- ϕ relationship expressed by Eq. (3.20).

For two magnetic fields of equal magni-

tude ($|B_1| = |B_2|$), the reconnection electric field can be written as

$$E_R = u_I B_I \sin \frac{\theta}{2} \quad (3.21)$$

where θ is the angle between the two fields (see Fig. 3.6a) (cf. Sonnerups 1974). This means that only the field components perpendicular to the X-line are allowed to reconnect. The electric field \vec{E}_R , parallel to the X-line, is the only component of the magnetosheath electric field to penetrate into the open magnetosphere (Kan and Lee 1979). The potential difference across the polar cap, ϕ_{pc} is due to the perpendicular component of \vec{E}_R , i.e. $E_R \sin \theta/2$ as shown in Fig. 3.6b. The polar cap potential can

then be written

$$\phi_{pc} = u_I B_I \sin^2 \frac{\theta}{2} l_R \quad (3.22)$$

where l_R is the effective length of the reconnection line.

The Joule heat dissipation in the polar cap ionosphere is given by

$$P = \frac{\phi_{pc}^2}{R} = u_I^2 B_I^2 \sin^4 \frac{\theta}{2} \frac{l_R^2}{2R} \quad (3.23)$$

where R is the ionospheric resistance.

Recently, Reiff et al. (1981) have computed the convection potential drop across the polar cap from data obtained on low altitude satellites and correlated with parameters measured simultaneously in the upstream solar wind. They found that the bulk of the potential drop and its variations with IMF parameters are successfully predicted by merging theory. A significant 'background' drop (~ 35 kV) does not depend on IMF parameters and was tentatively attributed to closed model processes such as viscosity and pressure gradient forces (cf. Sect. 3.3). The potential drop was found to be better correlated with IMF parameters than with geomagnetic activity indices. This was found reasonable because the latter are affected by non-linear responses of the magnetosphere to the polar cap input (cf. Sect. 3.4).

Concerning the spatial distribution of the potential inside the polar cap, the IMF B_Y component is considered an important parameter. When B_Y differs from zero the reconnection-line is inclined with respect to the equatorial plane. Thus the Lorentz force acting on the open field lines ($\vec{F} = \vec{J} \times \vec{B}_N$, where \vec{J} is the surface current flowing on the magnetopause and B_N is the component of the magnetic field normal to the magnetopause) has a longitudinal component which will produce zonal flow of field lines on the

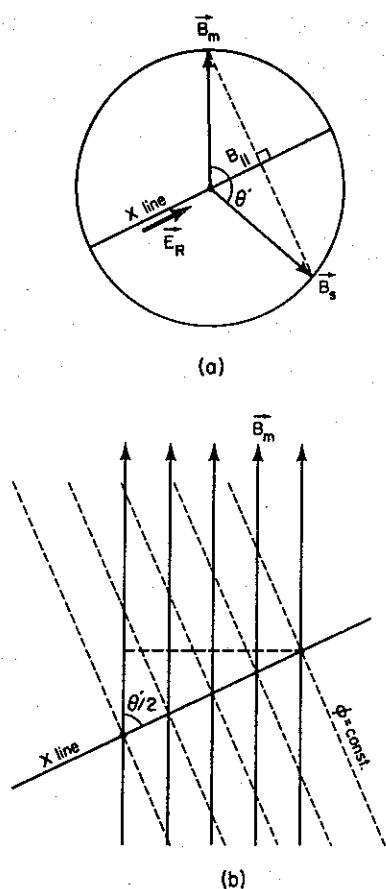


Fig. 3.6. A schematic illustration of the field line reconnection geometry for equal magnitude of the fields inside and outside the interface (\vec{B}_m and \vec{B}_s). (b) is an illustration of the equipotentials (dashed lines) of the reconnection electric field (Kan and Lee 1979).

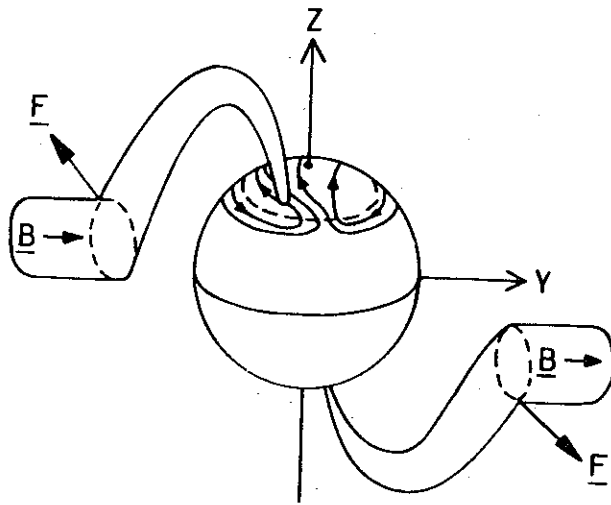


Fig. 3.7. Sketch illustrating the E-W forces F exerted on open flux tubes in the presence of an IMF B_Y field, resulting in a torque being exerted on the magnetosphere about the earth-sun line. The view is from the direction of the sun. Also illustrated is the resulting azimuthal flow in the dayside cusp region (Svalgaard-Mansurov effect) which implies asymmetric addition of flux tubes to the tail lobes under the action of the torque. The dashed line is the open field line boundary (Cowley 1981).

dayside edge of the polar cap (cf. Fig. 3.7). Reconnection with eastward IMF ($B_Y > 0$) causes field lines to be convected toward the west. Westward (eastward) convection will drive an eastward (westward) Hall current producing geomagnetic signatures denoted DPY (cf. Friis-Christensen and Wilhelm 1975). When $B_Y > 0$ ($B_Y < 0$) the size of the convection vortex (and equally the equipotential vortex and the equivalent current vortex) is expected to be enlarged (reduced) on the dusk side, but reduced (enlarged) on the dawn side. Ionospheric convection should be stronger on the afternoon side in the northern polar cap for $B_Y < 0$.

An important property of the open model of the magnetosphere is that the radius of the dayside magnetosphere (R) and the size of the polar cap will vary with IMF. According to observations (Aubry et al. 1970) the magnetopause shrinks without a significant

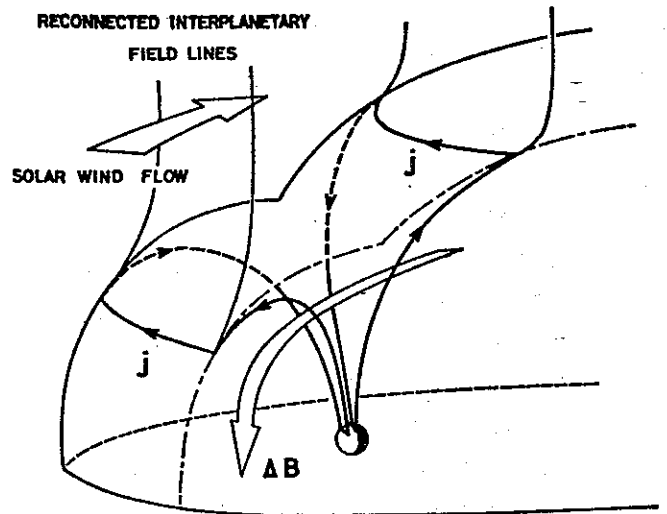


Fig. 3.8. Schematic illustration of the current system of the time of southward interplanetary magnetic field. When the reconnection of magnetic field lines occurs on the dayside magnetopause, magnetosheath plasma adjacent to the magnetopause is decelerated as its momentum is transferred to the ionospheric plasma. The corresponding polarization current flows along the magnetopause, which closes its circuit in the ionosphere via reconnected field lines. The resultant current circuit reduces the dayside magnetic flux as shown by a curved white arrow (Maezawa 1974).

change in the magnetic field jump (ΔB) across it. Consequently, the reduction of the total magnetopause current, δI_M , stems from a change in the meridional length of the magnetopause:

$$\delta I_M = \frac{\Delta B}{2\mu_0} \delta R \quad (3.24)$$

where δR is the change in the nose radius. Coroniti and Kennel (1973) take δI_M as an estimate of the decrement of the Chapman-Ferraro current (depicted as \vec{j} in Fig. 3.8). It is suggested that this current diminution provides the dominant current feeding the ionospheric Pedersen current. The magnetic field produced by this current system acts to reduce the geomagnetic field in the vicinity of the dayside magnetopause. The circuit may be regarded as a shunt introduced into the interplanetary electric field due to the contact with the ionosphere

through open field lines. The dissipation of the electric field energy by the shunting circuit is to be compensated by the deceleration of the solar wind flow. In the region where the deceleration occurs there exists an inertia current density given by:

$$\vec{j} = \frac{\rho}{B^2} \vec{B} \times (\vec{v} \cdot \nabla) \vec{v} \quad (3.25)$$

During slightly disturbed conditions the total current intensity is about 10^6 A. Since the scale of the dayside current loop is approximately $10 R_E$, the magnetic flux produced by the circuit is estimated to be of the order of 10^8 Wb. An erosion of magnetic flux of the order of 10^8 Wb taking place with constant efficiency over the sunward half of a circular belt of the dayside magnetosphere corresponds to inward/equatorward displacements of the magnetopause/cusp by $\sim 2.5 R_E/5$ degrees.

Response-times of the magnetosphere to variations of the IMF condition are briefly considered (cf. Nishida 1978, p. 79). The time in which the change of state of the dayside reconnection line is communicated to the ground, τ_1 , is given roughly by s/v_A , where s is the length of the geomagnetic field line reaching the reconnection line and v_A is the Alfvén speed. τ_1 is thus comparable to the transmission time of SI signals from the magnetopause to the ground, and is estimated to be around 1 min. A second characteristic time, τ_2 , arises from the motion of the magnetopause in response to IMF variations. The interplanetary electric field seen by the reconnection line is $(\vec{u}_I - \vec{u}_b) \times \vec{B}_I$ where \vec{u}_b is the velocity of the magnetopause. Thus the electric field applied on the reconnection line differs from $\vec{E}_I = -\vec{u}_I \times \vec{B}_I$ until the magnetopause current reaches the equilibrium intensity and the motion of the dayside magnetopause stops. According to Coroniti and Kennel (1973)

$\tau_2 \sim 400 \Sigma_p$ where Σ_p is the Pedersen conductivity (in mhos), and is estimated to be around ten minutes. This is comparable to the delay-time of ~ 15 min. found between IMF and its geomagnetic effects.

In recent years data from the frontside of the magnetopause which allow quantitative checks of the predictions of the macroscopic theory of reconnection have become available. The International Sun-Earth Explorers, ISEE-1 and -2, were the first satellites with the right orbits and instruments to observe effects of reconnection at the dayside magnetopause. Paschmann et al. (1979) have reported an event in which changes of flow momentum at the magnetopause near noon was consistent with a rotational discontinuity. According to this model the magnetic field changes direction by a large angle and has a finite component normal to the discontinuity. This is illustrated in Fig. 3.9

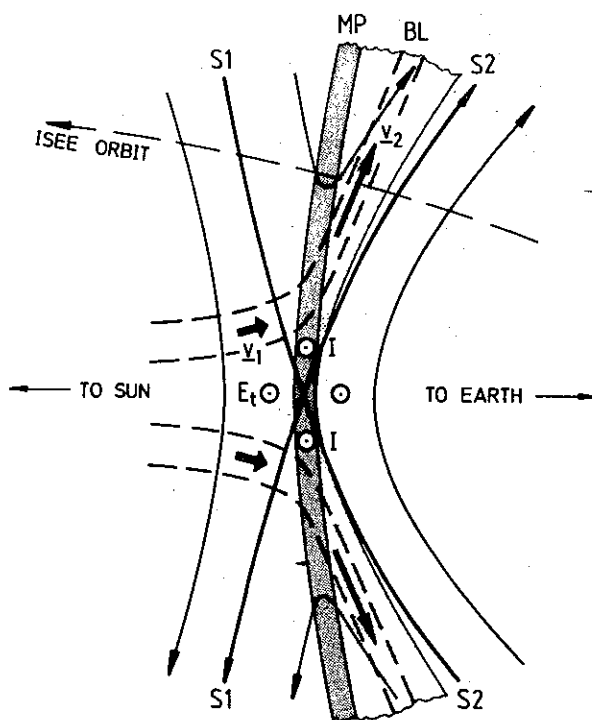


Fig. 3.9. Reconnection situation at the dayside magnetopause with southward pointing interplanetary field. The shaded area shows a layer of accelerated plasma flow after transition of the solar wind through the rotational discontinuity (Paschmann et al. 1979).

for the simple case of almost antiparallel fields. The plasma that transits through the discontinuity should be accelerated by an amount that is related to the balance of magnetic and mechanical stresses which (in an isotropic plasma) reads:

$$[\rho \vec{v}_t v_n] = \frac{1}{\mu_0} [\vec{B}_t B_n] \quad (3.26)$$

Index n and t refer to the normal and tangential components, respectively. Square brackets indicate the jump across the discontinuity. Since $B_n = \text{const.}$ and $\rho \cong \text{const.}$, we have the simple relations:

$$[\vec{v}_t] = \frac{[\vec{B}_t]}{\sqrt{\mu_0 \rho}} \quad (3.27)$$

$$v_n = \frac{B_n}{\sqrt{\mu_0 \rho}} \quad (3.28)$$

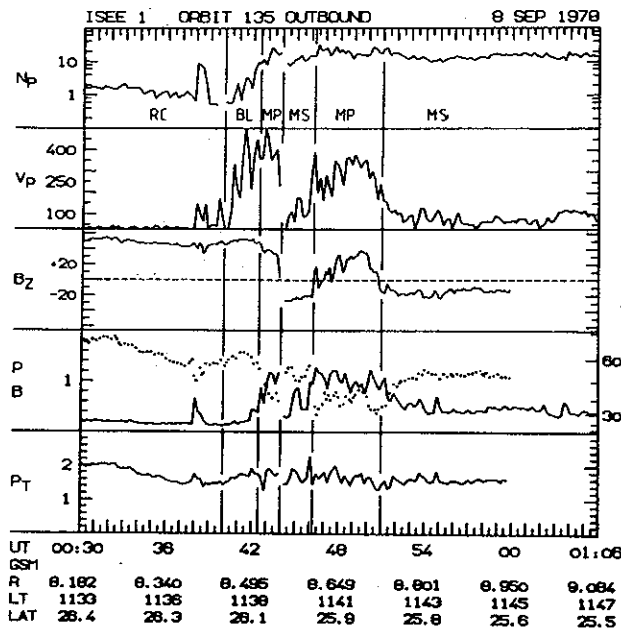
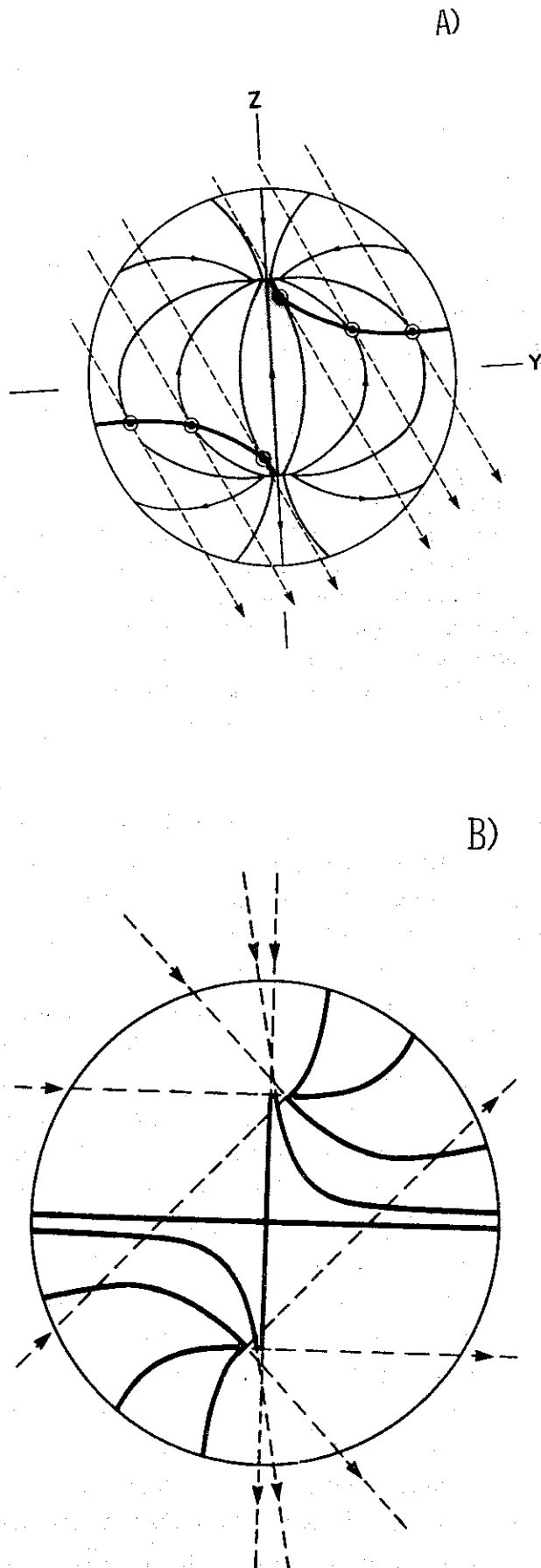


Fig. 3.10. Plasma and magnetic field data from a transition of ISEE 1 through the magnetopause near local noon. N_p , V_p , B_z , P , B , and P_T are plasma density, flow speed, component of B normal to the ecliptic, gas and magnetic pressures and the total pressure, respectively. The units are cm^{-3} , km/s , nT , and 10^{-7}Nm^{-2} . The symbols RC, BL, MP, MS designate the different plasma regimes encountered, namely ring current, boundary layer, magnetopause layer, magnetosheath (i.e. shocked solar wind) (Paschmann et al. 1979).

In several studies of plasma flow at the magnetopause (Heikkila 1975; Paschmann et al. 1976; Haerendel et al. 1978) it was quite disturbing that the predictions of Eq. (3.27) were not encountered even when the magnetic fields inside and outside the magnetopause were almost oppositely directed. It became evident that if reconnection occurred at all in the explored regions it must be transient and small-scale in nature and thus escape detection. The measurement of Paschmann et al. (1979) was sufficiently fast to cope with this difficulty. Figure 3.10 shows a set of data on three subsequent transitions through the magnetopause along a pass as sketched by the dashed line in Fig. 3.9. The most important feature is the large increase of plasma flow velocity by several 100 km/s just inside the magnetopause. Via density measurements and the magnetometer data, Eq. (3.27) was checked. Agreement was found within 10%, which was considered rather good in view of several sources of experimental error. About 10 events of this kind have been identified, which is $\sim 30\%$ of the total number of cases in which the orientation of the IMF was favorable for reconnection. Thus, strong antiparallel field components are apparently not sufficient for the process to occur. What a sufficient condition could be, is not known yet (Haerendel 1980).

Reconnection near the cusps. Geometrical considerations presented by Crooker (1979) show that dayside magnetic merging, when constrained to regions where the fields are antiparallel, results in two separate reconnection lines that converge at the polar cusps (cf. Fig. 3.11a). From Fig. 3.11a we also note that for IMF $B_Y \neq 0$, closed field lines constitute the subsolar region of the magnetopause. Reconnection in this region is restricted to IMF due south. For all other cases, no reconnection occurs in a lune-like



area centred on the noon-midnight meridian. The width of the region not subject to erosion increases with increasing deviation of the IMF from due south (Fig. 3.11). According to this model the cusp region seems to be the primary site of the reconnection process. This is consistent with the referred lack of observations of accelerated flow along the dayside magnetopause (as predicted for merging near the subsolar point). The dayside merging configurations proposed by Crooker (1979) predict polar cap convection patterns (cf. Fig. 3.12) which are confirmed by observations. Among these are the asymmetric double cells where the strongest convection occurs on the side of the polar cap opposite to the direction of the IMF B_Y component (Heppner 1972; Mozer et al. 1974; Berthelier et al. 1974). The convection gaps shaded in Fig. 3.11 are consistent with the sense of field-aligned cusp currents observed by Iijima and Potemra (1976).

3.3 The closed magnetosphere—the low-latitude boundary layer

A different mode of solar wind-magnetosphere interaction, based on a closed model of the magnetosphere, is discussed by Heikkilä (1978). A closed magnetosphere means that there is no direct interconnection between the interplanetary and the earth's magnetic field. In such a situation the mag-

Fig. 3.11. Schematic view from the sun of the dayside magnetopause. (a) Earth field lines (solid) converge in a cusp-like configuration. Merging lines (heavy solid) are the locus of points where the interplanetary field lines (dashed) are antiparallel to the earth field lines. The shaded area contains no points where the interplanetary and earth fields are antiparallel. (b) Merging lines (solid) for various orientations of the interplanetary magnetic field (dashed lines). Merging lines are constructed according to the method illustrated in (a) (Crooker 1979).

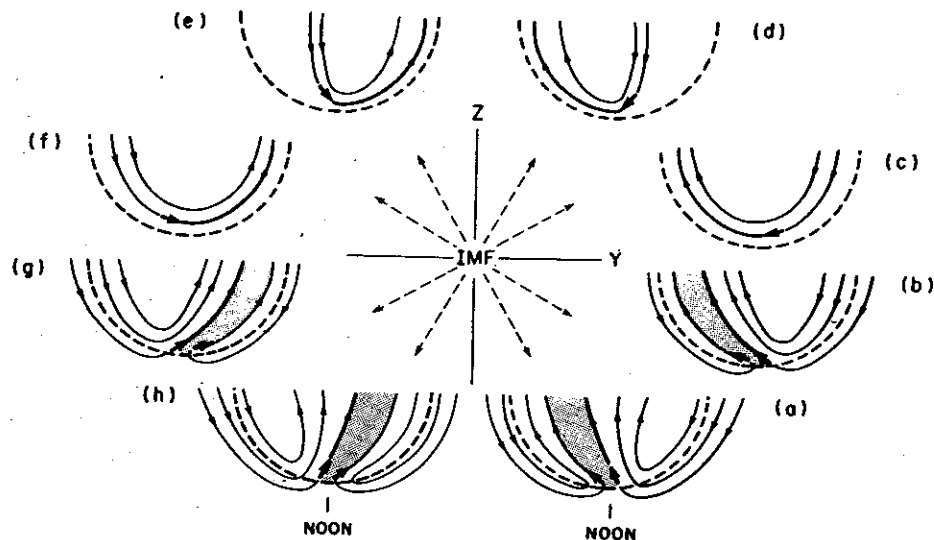


Fig. 3.12. Predicted polar cap convection patterns in the dayside northern hemisphere, viewed from above, for various orientations of the interplanetary magnetic field (IMF) in the Y-Z plane, perpendicular to the earth-sun line. The short heavy arrows represent the direction of flow initiated by dayside merging near the cusp. Note the pattern of rotation of the arrows around the figure in response to the rotation of the IMF. The heavy streamlines in each pattern indicate the position of maximum convection. Those streamlines which cross the polar cap boundary (the heavy dashed line) effect a transfer of flux from closed dayside field lines to open tail lobe field lines. The shaded regions are convection gaps (Crooker 1979).

netopause will be an equipotential surface. Observations from satellite-crossings of the magnetopause indicate that the low-latitude region of the magnetopause often is a nearly equipotential surface. Electric field components tangential to the dayside magnetopause are seldom observed (cf. Heikkila 1978).

For the magnetopause to be an equipotential surface in the presence of an external electric field, within the magnetosheath, a surface charge distribution as shown in Fig. 3.13a, for a southward IMF, is necessary. Negative charges are needed on the dawnside to provide terminations for the magnetosheath field, and similarly, positive charges are needed on the duskside as sources for the continuation of the external field.

Inside an equipotential surface there can be no electric field unless there exist separate

sources for the internal field. Thus, the dawn-dusk magnetosphere field must be due to positive charges somewhere near, but inside the magnetopause on the morning side and negative charges toward the dusk side. The resulting polarized boundary-layer can transfer the external magnetosheath electric field into the magnetosphere. As indicated in Fig. 3.13, the flow of plasma inside the boundary layer is tangential to the frontside magnetopause. This requires a $\vec{J} \times \vec{B}$ -force pointing inward on both the dawnside and the duskside, and thus a westward current. Near the throat region on the dayside this current flows against the electric field owing to the inner charge layer; this region therefore has a negative $\vec{E} \cdot \vec{J}$ and acts as a generator (cf. Heikkila 1978).

Since field-aligned currents (J_{\parallel}) are required along any boundary where the horizontal ionospheric current diverges, the

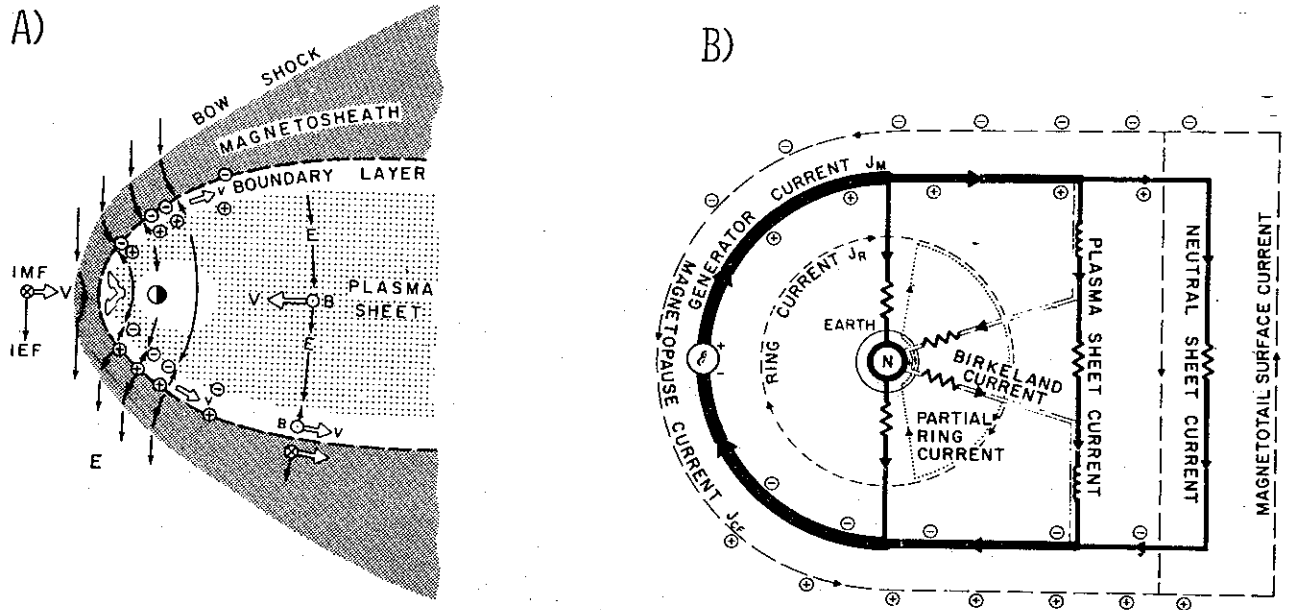


Fig. 3.13. (a) With an equipotential magnetopause an electric field inside the magnetosphere can exist only if separate sources exist owing to charges placed as shown. The sheet densities need not all be the same; thus the boundary layer and magnetopause region can be viewed as a combination of a charge sheet and a dipole sheet. (b) Geometry and circuit aspects of important magnetospheric currents. Flow of the boundary layer plasma around the curved magnetopause implies a westward current. In the dayside region this current opposes the electric field and thus acts as a generator (Heikkila 1978).

polarized layer has been suggested as a source of J_{\parallel} (e.g. Boström 1977):

$$\begin{aligned} J_{\parallel} &= \nabla \cdot \vec{J}_{\perp} \\ &= \Sigma_p \nabla \cdot \vec{E}_{\perp} + \vec{E}_{\perp} \cdot \nabla \Sigma_p \\ &+ \vec{B} \times \vec{E} \cdot \nabla \Sigma_H \end{aligned} \quad (3.29)$$

According to Eastman et al. (1976) some of the forward momentum of the boundary layer plasma flow is converted to the electrical load in the ionosphere when the polarization charge is drained by depolarizing current flow along field lines. Thus, the boundary layer constitutes a magneto-hydrodynamic generator (see Fig. 3.14).

When traversing the boundary layer from the magnetosheath to the magnetosphere, the bulk plasma velocity decreases from the antisunward solar wind velocity at the magnetopause to zero at the inner edge and reverses to sunward flow in the magnetosphere. If we assume frozen-in field lines, we can map this flow to the ionosphere,

resulting in the familiar two-cell convection pattern. The ion convection reversal in the ionosphere then maps to the inner surface of the equatorial boundary layer.

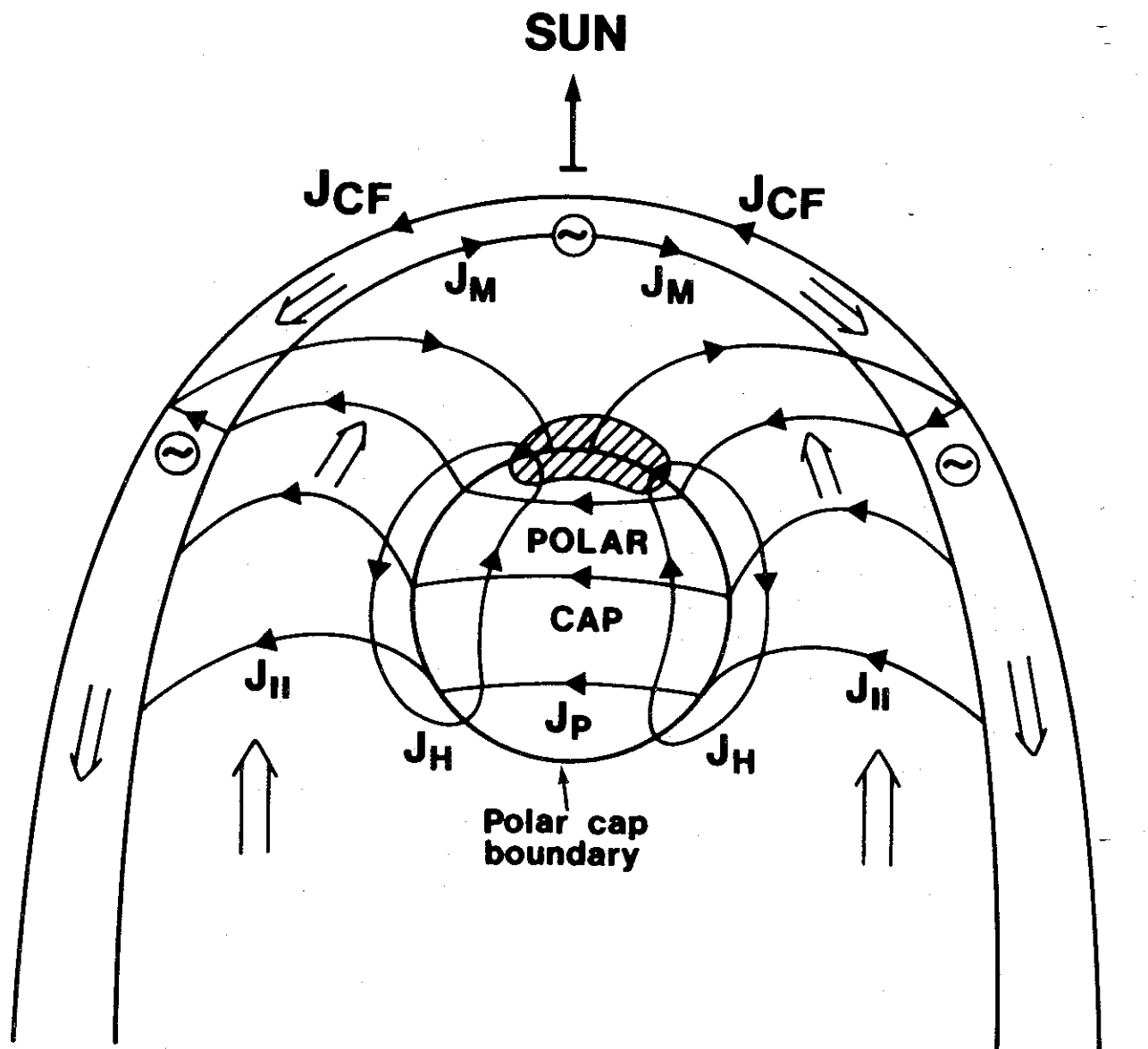
An idealistic model description of the low latitude boundary layer (LLBL) is given by Sonnerup (1980). A one-dimensional version of the law of conservation of x-momentum in the boundary layer can be written (see Fig. 3.15):

$$\begin{aligned} \rho \frac{dv_x}{dt} &= \rho v_y \frac{dv_x}{dy} \\ &= (\vec{j} \times \vec{B})_x + \mu \frac{d^2 v_x}{dy^2} \end{aligned} \quad (3.30)$$

where μ and ρ are the viscosity and density, respectively. The term on the left represents convective momentum transfer caused by a mass diffusion flux ρv_y across the layer:

$$\rho v_y = -D \frac{d\rho}{dy} \quad (3.31)$$

where D is the diffusion coefficient and ρ is



- ⊗ Magnetopause boundary layer dynamo ($\vec{E} \cdot \vec{J} < 0$)
- ▨ Polar cusp "midday gap"
- Electric currents
- ⇒ Plasma flow

Fig. 3.14. Sketch view of a proposed current system based on models by Heikkila (1978) and Eastman et al. (1976). It consists of Pedersen (J_p) and Hall (J_H) components in the polar ionosphere as well as field-aligned currents (J_{II}) connecting the ionosphere with currents flowing along the inner and outer edges of the magnetopause boundary layer (J_M , J_{CF}). For simplicity the ring current and the 'Region 2' field aligned current are not included. The figure is not in scale.

the density of diffusing magnetosheath-like plasma. The first term in the right side of (3.30) is given by $-\sigma v_x B^2$ where σ is an effective electrical conductivity. The last term represents the viscous force per unit volume.

Viscous model of the low-latitude boundary layer

A simple, purely viscous model with no mass diffusion (vanished left-hand side of (3.30)) gives the velocity-profile:

$$v_x = -v_0 e^{-y/\delta_v} \tag{3.32}$$

where v_0 is the maximum boundary layer speed ($y = 0$) and δ_v is a characteristic viscous length defined by $\delta_v = (\mu/\sigma B^2)^{1/2}$.

With a kinematic viscosity $\nu_k = \mu/\rho_0 = 10^9 \text{ m}^2/\text{s}$, a boundary layer density $\rho_0 = 10 \text{ protons cm}^{-3}$, $v_0 = 200 \text{ km/s}$, $\sigma = 5.96 \times 10^{-8} \text{ mho/m}$, and $B = 30 \gamma$, one finds $\delta_v = 558 \text{ km}$. This value is a few times smaller than observed boundary layer thicknesses on the magnetospheric flanks (Eastman and Hones 1979). The velocity profile is a decaying exponential in which the flow speed falls to 14% of v_0 in a distance of $2\delta_v$. The total voltage across the boundary layer

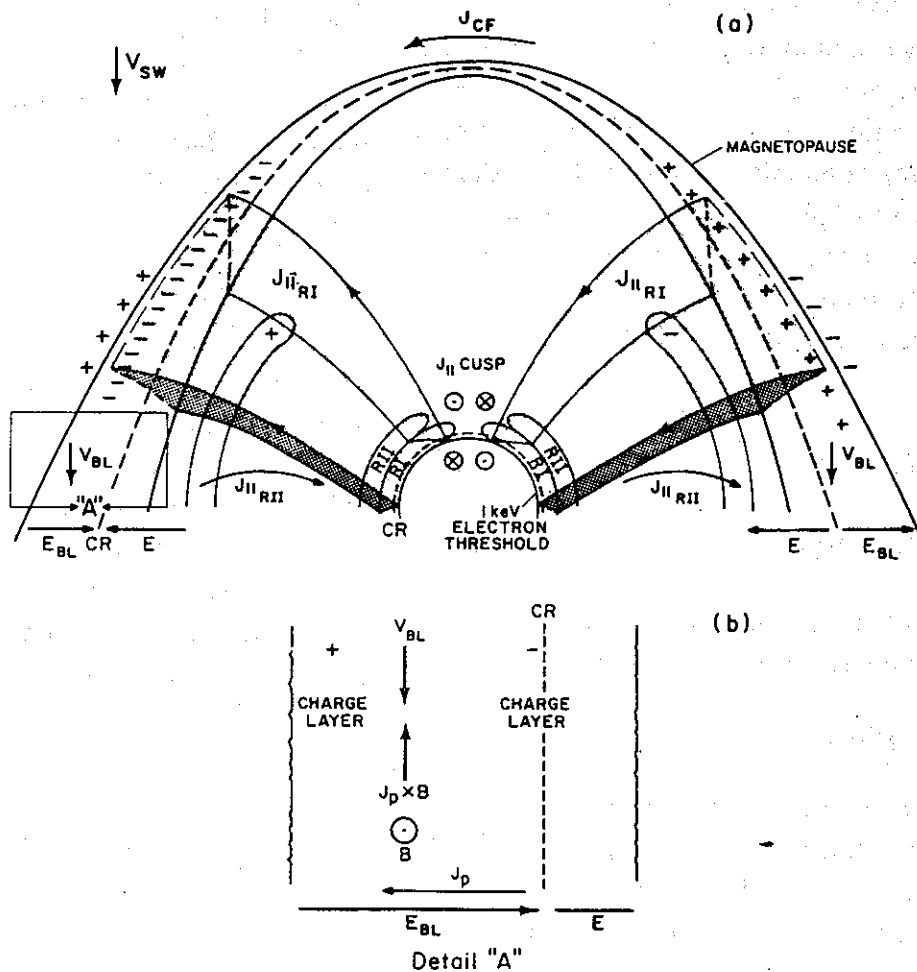


Fig. 3.15. (a) A schematic diagram of the dayside magnetosphere showing 'Region 1' currents flowing to and from the boundary layer. The dashed line locates the plasma convection reversal in the ionosphere and the magnetosphere. The poleward solid line indicates the 1-keV electron limit in the ionosphere and is mapped to the outer edge of the boundary layer. (b) An expanded view of the boundary layer region in Fig. a (Bythrow et al. 1981).

is:

$$\Delta\phi_{BL} = v_0 B \delta_v = 3.3 \text{ kV}$$

In this numerical example only 10–15% of the total potential drop across the magnetosphere occurs in the boundary layers; the remainder occurs across the open polar cap field lines.

Diffusion model of the boundary layers

Published equatorial boundary layer profiles (Eastman et al. 1976; Haerendel et al. 1978) indicate that the plasma density usually tends to fall off to the background level at approximately the same place as that where the plasma flow speed becomes insignificant. A purely viscous model does not produce such a result. Secondly, there is direct evidence of a certain amount of interpenetration of boundary layer plasma and hot low-density 'ring current' plasma (Haerendel et al. 1978).

Mass conservation in a two-dimensional model leads to the following formulas when combined with Eq. (3.31) (cf. Sonnerup 1980):

$$\rho/\rho_0 = (1 - y/\delta_p)^{\frac{2}{m+1}}; \quad m \neq -1 \quad (3.33)$$

$$v_{y0} = (2D_0/\delta_p)/(m+1) \quad (3.34)$$

where it has been assumed that the diffusion coefficient depends on density as follows:

$$D = D_0(\rho/\rho_0)^m$$

D_0 is the value of D at $y = 0$, where $\rho = \rho_0$. The quantity δ_p is referred to as the 'precipitation length' because on this scale length particles are removed from the equatorial regions by flow-along field lines toward higher latitudes.

Omitting the viscous term and with ρv_y replaced by

$$\rho v_y = \rho_0 v_{y0} (1 - y/\delta_p) \quad (3.35)$$

Equation (3.30) is integrated to yield:

$$v_x/v_0 = -(1 - y/\delta_p)^\alpha \quad (3.36)$$

where

$$\begin{aligned} \alpha &= (\sigma B^2 \delta_p / \rho_0 v_{y0})^{\frac{1}{2}} \\ &= \delta_p \left(\frac{\sigma B^2 / (m+1)}{2\rho_0 D_0} \right)^{\frac{1}{2}} = \left(\frac{\delta_p}{\delta_d} \right) \end{aligned}$$

The quantity δ_d is called the 'diffusive length' and is defined by

$$\delta_d = \left(\frac{2}{m+1} \frac{\rho_0 D_0}{\sigma B^2} \right)^{\frac{1}{2}}$$

From (3.33) and (3.36) it is seen that ρ and v_x drop to zero at the same place ($y = \delta_p$). Theoretical information concerning the m value can be obtained only by a study of the microprocesses responsible for the diffusion, but on the basis of observed density profiles a value of m near unity appears reasonable (Sonnerup 1980).

On the IMF control of electric coupling through the low-latitude boundary layer

The boundary layer processes described above are generally thought to be independent of IMF and thus may constitute the principal transfer mechanism during northward IMF when magnetic reconnection does not exist. According to Eastman et al. (1976) it is not clear how LLBL processes are affected by a southward IMF.

Piddington (1979) has a qualitative explanation for the IMF control of geomagnetic activity in terms of the boundary layer model. According to him, the region of transition from the IMF to the magnetosphere has very different properties for parallel and antiparallel magnetic fields. In the latter case there is a layer of non-magnetic plasma whose particles are not trapped in either of the two magnetic structures, but bounce back and forth, penetrating each in turn. These motions are likely to provide momen-

tum transfer and hence frictional interaction. A southward interplanetary magnetic field, with its associated dawn-to-dusk electric field, means that the interplanetary medium is electrically connected to the magnetosphere through magnetic neutral sheets. In the case of parallel IMF and magnetosphere magnetic fields their respective plasma particles are trapped and isolated from one another. There is little frictional interaction and a poor electrical connection. Thus, when the external electrical field is reversed (northward IMF), it is simultaneously disconnected from the magnetosphere.

Following these arguments of Piddington (1979), it seems reasonable that both the diffusion- and viscosity terms of Eq. (3.30) are enhanced by a southward turning of the IMF. Consequently, the momentum-transfer to the boundary layer is increased ($\Delta|v_x| > 0$) and so is the efficiency of the boundary layer dynamo. This means an increased electrical energy input to the polar ionosphere with associated geomagnetic effects.

As described in Sect. 3.2, the enhanced solar wind-magnetosphere coupling due to magnetic reconnection is another very important mechanism for transfer of plasma, momentum and energy for southward IMF.

The boundary layer and field aligned currents
According to the model of Eastman et al. (1976), any point near the outer edge of the boundary layer projects along field lines to the polar ionosphere near noon. Points deeper within the boundary layer project to nearly the same latitude, but to positions that are displaced increasingly from local noon with increasing inward penetration into the boundary layer (see Fig. 3.14). The energies of the particles producing these field-aligned currents should be characteristic of the boundary layer and should

increase with increasing distance from local noon (corresponding to the observations of increasing thermal energy during inbound satellite-crossings of the layer) (cf. Eastman and Hones 1979—their Figs. 2 and 6). The cusp precipitation region is regarded to be the ionospheric projection of the outer part of the boundary layer. This conclusion is supported by the similarity of boundary layer and low altitude cusp electron spectra (cf. Eastman et al. 1976).

Field-aligned currents (FAC's) are considered an important channel of energy-transfer between the boundary layers and the high-latitude ionosphere. The global morphology of the two major high-latitude field-aligned current systems, 'Region 1' and 'Region 2', is now well established (Iijima and Potemra 1976a). The field aligned current system associated to the low-latitude boundary layer dynamo should lie along the auroral oval sunward of the Birkeland-current associated with the magnetotail dynamo (Roederer 1980).

Bythrow et al. (1981) observed 'Region 1' currents to span the convection reversal associated with the polar cap boundary and to extend approximately 0.5 degrees poleward of the reversal. The poleward edge of the 'Region 1' currents are observed to be nearly coincident with the 1 keV threshold level in the satellite particle spectrograms. It has been argued that this marks a low-latitude limit of open field lines; hence the 'Region 1' currents flow along closed field lines and extend about 0.5° into a region of antisunward plasmaflow (see Fig. 3.15). The observations reported by Bythrow et al. (1981) are consistent with a model in which the dayside 'Region 1' currents have a source that is at least partially due to 'viscous-like' interaction in the low-latitude boundary layer.

The total 'Region 1' FAC between

1200 MLT and 1800 MLT (I_{\parallel}) must be equal to the total polarization current across the corresponding section of the boundary layer. Observations of the ionosphere show that I_{\parallel} is of the order of 10^6 A, which requires electrons to flow out of the boundary layer or be replaced at its surface at the rate of 10^{25} s $^{-1}$. This is only 1% of the flow rate of particles through a cross-section of the boundary layer. Therefore, no significant reduction in the bulk flow velocity in the boundary layer would result if it were the source of 'Region 1' currents (Bythrow et al. 1981).

The 'Region 2' FAC's are entirely equatorward of the convection reversal and are thus associated with sunward convecting plasma on closed field lines.

3.4 Non-linear responses of the magnetosphere to solar wind energy input-magnetospheric substorms

The stationary and quasi-stationary processes discussed in Sects. 3.2 and 3.3 describe a rather continuous energy dissipation providing the quiet time auroral oval and the associated ionospheric current system S_q^p . The quiet time oval is caused by precipitating particles with a total power of $\sim 5 \times 10^9$ W (Murphree and Anger 1978). A typical value of the energy dissipated in the polar ionosphere by the S_q^p current (cf. Sect. 5.2) is $\sim 5 \times 10^{10}$ W corresponding to the current intensity 5×10^5 A, the polar cap electric field 20 mV/m and 3000 km as the diameter of the polar cap (cf. Akasofu 1977 p. 52).

The amount of transfer of energy and momentum to the magnetosphere is controlled by solar wind conditions (cf. Sect. 3.2). Increased efficiency of the solar wind-magnetosphere dynamo results in increased intensity in the magnetosphere-ionosphere current circuits. Akasofu (1980) summarizes the following responses of the

magnetosphere to the so-called 'sharp southward turning' of the IMF vector:

- a) Inward shift of the dayside magnetopause,
- b) Equatorward shift of the cusp,
- c) Changes of the radius of the magnetotail cross-section,
- d) Changes of the thickness of the plasma mantle,
- e) Changes of the high latitude lobe field,
- f) Changes of the thickness of the plasma sheet,
- g) Equatorward expansion of the auroral oval,
- h) Increase of the electric field across the polar cap,
- i) Enhancement of the S_q^p variations,
- j) Enhancement of plasma convection,
- k) Occurrence of a magnetospheric substorm,
- l) Occurrence of a magnetospheric storm.

In spite of these magnetospheric responses, the correlation coefficient between the IMF B_z and the auroral electrojet index AE is only of the order of 0.4–0.5 (Akasofu 1980). This indicates that the geomagnetic activity as reflected by the AE index does not respond linearly to IMF variations.

When the solar wind-magnetosphere dynamo efficiency increases above a certain critical value, the quasi-stationary mechanisms for the energy-transfer cannot dissipate the increased power fast enough. As a result, the magnetosphere develops suddenly an efficient mode of energy dissipation which is identified as the magnetospheric substorm. One way of increasing the energy-dissipation is to bring the cross-tail current to the ionosphere, where Joule-heat dissipation can take place.

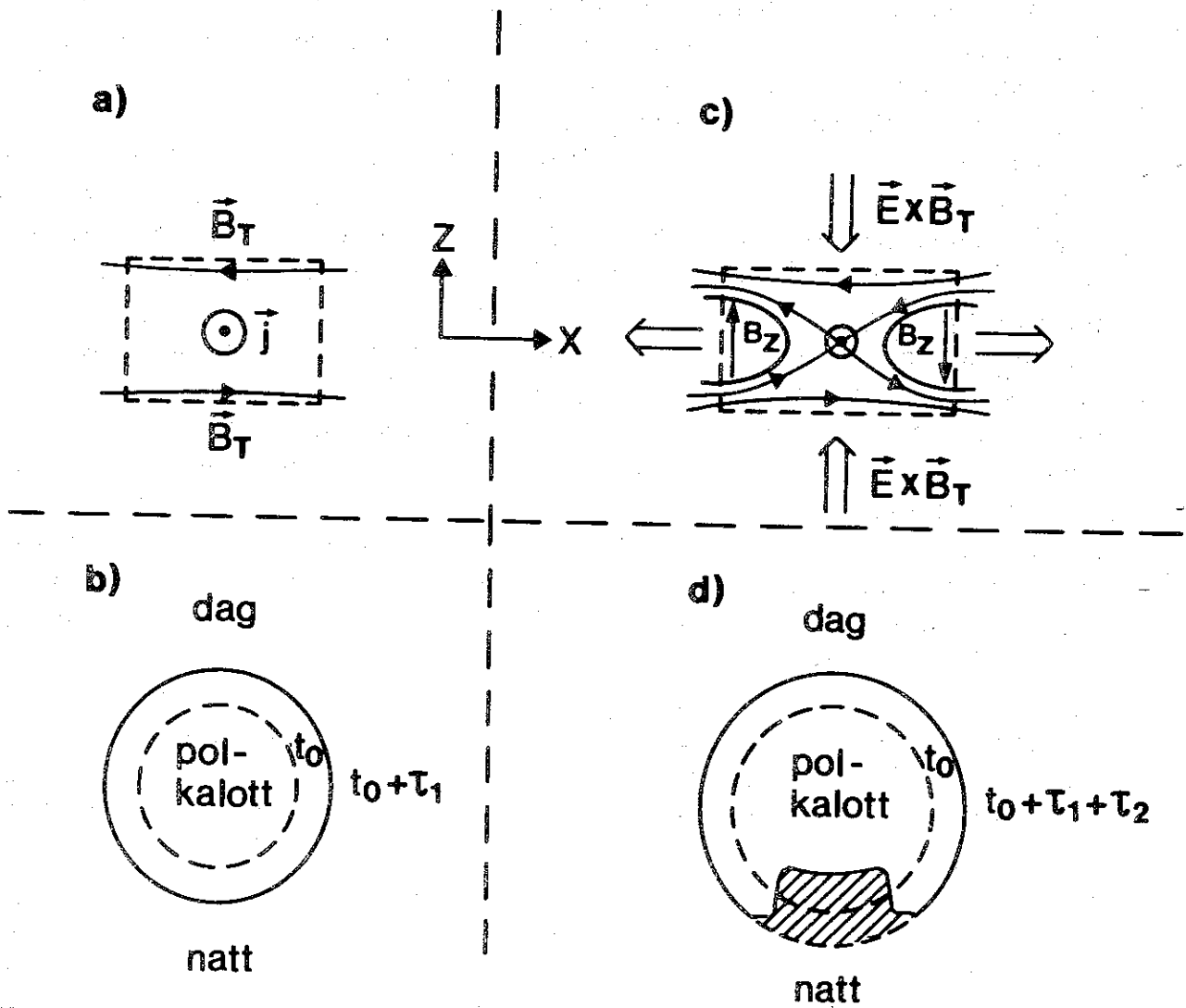
A schematic illustration of a postulated topological magnetotail development during

substorms is shown in Fig. 3.16. The formation of a new X-line at some place in the magnetotail and the related transition from a tail-like to a more dipole-like field configuration are associated with a reduction of the cross-tail electric current.

This is seen if one considers the Ampèrian integral $\oint \vec{B} \cdot d\vec{l}$ around a rectangular loop enclosing the X-line (cf. Fig. 3.16) and note that the formation of the X-line produces

non-zero B_z and thus negative contributions from both side segments, while to first order it has little effect on the positive contributions from the top and bottom segments.

To maintain continuity as the current across the magnetotail is reduced, it is widely assumed that the current has been diverted along field lines and flow through the ionosphere, most likely as the westward auroral electrojet (Vasyliunas 1980). To drive the



$$\tau_1 \sim 40 \text{ min.}; \tau_2 \sim 20 \text{ min.}$$

Fig. 3.16. Magnetotail magnetic field topologies. The stretching towards more tail-like field lines (a) corresponds to the expansion of the auroral oval (b). The transition to more dipolar field (c) corresponds to the poleward expansion of nightside auroral forms (d).

current through the ionospheric resistance, an electric field is needed, which may in turn be mapped out along field lines—the ionosphere becomes a voltage source for the magnetotail. This electric field has a dawn-to-dusk component and is therefore associated with plasma flow toward the X-line from above and below, as shown in Fig. 3.16c.

The possibility of a positive feedback mechanism thus becomes apparent, whereby the diversion of current from the plasma sheet to the ionosphere enhanced the plasma flow, leading to larger B_z and a further reduction of cross-tail current (Vasyliunas 1980). A threshold value of the solar wind-magnetosphere dynamo (cf. Sect. 3.2) of the order of 10^{11} watt has been related to the onset of this chain of positive feedback processes (i.e. the magnetospheric substorm) (cf. Akasofu 1980).

A magnetospheric substorm is defined as 'a transient process, initiated on the night-side of the earth in which a significant amount of energy derived from the solar wind-magnetosphere interaction is deposited in the auroral ionosphere and in the magnetosphere' (Rostoker et al. 1980). The onset of this process is most clearly signalled by explosive increases in auroral luminosity in the midnight sector. The level of energy dissipation is determined by the combination of auroral luminosity/ionization and electric fields (both primary and polarization fields).

The magnetotail development (Fig. 3.16) accounts qualitatively for several observed properties of auroral and geomagnetic activity during substorms (cf. Vasyliunas 1980). However, a main controversy still exists concerning the substorm. Is it initiated primarily by a local instability in the magnetotail or is it driven directly by an external solar wind variation?

According to McPherron (1979) a regular magnetospheric substorm appears to have

three phases: a 'growth phase' in which energy is extracted from the solar wind and eventually stored in the magnetotail; an expansion phase in which energy is explosively released; and a recovery phase in which the magnetosphere relaxes to a quiet state. Presently there is general agreement on the sequence of events, but not the name. The primary objection is that it has not been conclusively demonstrated that the expansion phase is a causal consequence of the 'growth phase' processes. Thus, Akasofu (1975a) and Kamide and Matsushita (1978) refer to these processes as the 'IMF effect' not to be included in the description of the cyclic evolution of the substorm.

In this report we will use the substorm concept as it was defined by Rostoker et al. (1980), which 'represents a consensus reached by nine magnetospheric physicists active in the field of substorm research'. Following that definition, neither the so-called 'convection bay' nor the 'growth phase', both characterized by enhanced quiet-time processes with no impulsive activity in the midnight sector, is to be included in the substorm concept. For details on the geomagnetic signatures of magnetospheric substorms, cf. Sect. 5.2.

4. EXPERIMENTAL RESULTS

4.1 *Morphology and spectral characteristics of dayside auroral emissions*

The photometer observations of midday aurora shown in Fig. 2.2 differ considerably from those taken on the nightside (e.g. Romich and Belon 1967a, b), where the 4278 Å traces follow almost exactly those of the 5577 Å emission. In Fig. 2.2 we observe that the 6300 Å and the 4278 Å traces peak towards the zenith from the 5577 Å peak. The observed separation between the different photometer traces indicate different

Table 4.1
List of observations of dayside auroras from Longyearbyen

Event No.	Time (UT) Date/hour/min/sec	Position peak intensity (el. from north horizon)		Solar depr. angle (deg.)	Geom. shadow height ~ peak intensity (km)		Height of peak intensity (km)		Spatial extension of luminosity (km)		Sunlight condition	Peak intensity (R)		Intensity ratios			
		6300 Wavelength (Å)	4278 Wavelength (Å)		6300 Wavelength (Å)	4278 Wavelength (Å)	6300 Wavelength (Å)	4278 Wavelength (Å)	6300 Wavelength (Å)	4278 Wavelength (Å)		6300 Wavelength (Å)	4278 Wavelength (Å)	R ₁	R ₂	R ₃	
1	Dec.10-05-08-15	91	4278		6300	4278	6300	4278	6300	4278	d	6300	4278	5577	6300	5577	6300
2	Dec.10-05-08-37	39	32	-21,4	470	1258	180	150	210-400 70	140-270 70	d	1970	40	350	50	9	5,6
3	Dec.10-05-10-30	37	30	-21,4	908	1459	190	160	130-170 35	130-220 45	d	2050	125	920	16	7	2,2
4	Dec.10-05-10-30	86		-21,4	976		260		180-420 60		d	1750	105	1200	17	11,4	1,4
5	Dec.10-05-11-20	82		-21,4	484		250		170-400 70		d	3075	80	830	38	10,4	3,7
6	Dec.10-05-11-20	35	28	-21,4	498	1780	190	170	140-240 30		d	2750	45	430	61	9,5	6,4
7	Dec.17-07-01-15	125	125	-16,9	1063	237	470	420	270-800 260	275-650 120	d	2000	100	1080	20	10,8	1,8
8	Dec.17-07-05-40	123	117	-16,7	237	301	510	580	350-800 330	500-800 260	s	5880	195	<100	30	<1	>55
9	Dec.17-07-30	130	130	-15,7	200	200	450	450	270-730 190	350-700 70	s	4540	135	<100	33	<1	>45
10	Dec.17-07-35	120	118	-15,5	207	209	350	300	170-440 100	180-470 60	s	3400	120	190	28	1,6	18
11	Dec.19-07-22-40	100	99	-16,0	234	235	260	310	190-500 100	200-500 70	s	8000	470	880	17	1,9	9
12	Dec.19-08-20-29	79	81	-14,0	205	203	315	325	250-500 110		ps	8420	390	2230	22	5,7	3,8
13	Dec.19-08-20-59	77	79	-14,0	207	205	350	350	300-500 100		s	2850	135	280	21	2,1	10
14	Dec.19-08-23-53	72	73	-13,9	209	208	320	320	260-460 75	250-500 55	s	2350	90	180	26	2,0	13
15	Dec.19-08-24-16	70	73	-13,9	211	208	300	325	210-500 75	230-400 60	s	3570	165	350	21	2,1	10
16	Dec.19-08-25-20	69	70	-13,9	211	208	300	300	200-600 95	200-550 85	s	3180	160	320	10	2,0	10
17	Dec.18-11-54-55	90	90	-12,0	142	142	220	220	160-320 80		s	3840	210	670	18	3,2	5,7
18	Dec. 9-12-13-35	62	54	-11,7	151	159	190	140	150-350 70	120-360 55	ps	3300	760	1270	4,3	1,7	2,6
19	Dec. 9-12-14-37	65	59	-11,7	149	154	200	140	160-430 80	120-400 70	ps	4390	580	3980	7,6	6,9	1,1
20	Dec. 9-12-45	73	68	-12,4	163	167	165	140	150-300 120	125-250 55	ps	6130	1060	7080	5,8	6,7	0,9
												3680	830	7580	4,4	9,1	0,5

emission altitudes. Since the geometric shadow height in the direction of maximum luminosity at 6300 and 4278 Å is 210 km for the event shown in Fig. 2.2, both these emissions come from the sunlit part of the ionosphere. Thus, most of the 200 R of the 4278 Å emission is sunlight resonantly scattered from N_2^+ ions. Other examples of completely and partly sunlit midday auroras are shown in Fig. 4.1.

Table 4.1 gives an overview of 20 triangulated auroral forms observed in Dec. 1979 with information on position, geometrical shadow height, absolute intensities, and intensity ratios. The events are arranged from 1 to 20 according to the local time of observation, extending from the morning to the post-noon sector covering an interval of ± 4 hours around local magnetic noon (09 UT). The solar depression angle varies between -11.7° and -21.4° . The geometrical shadow height corresponding to the

direction of maximum luminosity at 6300 Å varies between 142 and 1063 km with the darkness extending to larger altitudes at smaller elevations from the north horizon in the morning sector. Local solar noon is at 11 UT.

The uncertainty of the measured emission-altitudes, which depends on the altitude and the position of the auroral form relative to the observing sites, is estimated to be generally within ± 20 km. We notice that the maximum emission rate of the red line changes between 165 and 510 km. During sunlit conditions the altitude of the 4278 Å emission follows the red line fairly well. In cases of discrete forms in a dark atmosphere the nitrogen band as well as the green line are emitted lower down than the red line. Typical altitudes of maximum emission are between 140 and 160 km. The listed intensity ratios correspond to peak intensities uncorrected for atmospheric extinction.

Table 4.2

Characteristics of dayside auroras

Dayside auroral category	Observations (events)	Local time (geomagnetic)	I_{\max} (6300) (kR)	I_{\max} (5577) (R)	$R_3 = \frac{6300}{5577}$	Characteristic energy E'_0 (keV)
I	1 - 6	pre-noon	2 - 3	300 - 1000	1 - 5	$< 0,5$
II	7 - 16	midday	2,5 - 8	$< 100 - 900$	≈ 10	$\approx 0,1$
III	18 - 20	post-noon	3,5 - 6	4000 - 7500	0,5-1	$0,2 < E'_0 < 0,7$

	H_{\max} (6300) (km)	Width of 6300 Å emission (km)	Sunlight condition
I	180 - 260	60 - 70	dark
II	300 - 510	75 - 330	sunlit
III	165 - 200	70 - 120	partly sunlit

We note a large increase of the ratio $R_3 = 6300 \text{ \AA}/5577 \text{ \AA}$ at high altitudes.

The essential information in Table 4.1 is extracted and given in Table 4.2. Estimates of characteristic energy levels of the precipitating particles, assumed to be Maxwellian, are included. This is based on the intensity ratio R_3 combined with absolute intensities and applied to the model of Rees and Luckey (1974).

We are aware that general conclusions concerning the local time variation of spectral characteristics cannot be drawn from only 20 selected events. However, we have the general impression that the presented data illustrate some typical variations of the auroral condition at 75° latitude when the observing site rotates with the earth from the morning through midday and into the post-noon sector.

The highest altitude of auroral emissions corresponding to the softest particle spectrum (low E_0) is observed around geomagnetic noon. In this period the light emission takes the form of a quiet $\sim 100\text{--}300$ km broad belt of subvisual intensity (category II in Table 4.2). The auroral spectrum is dominated by the red oxygen lines at $6300/6364 \text{ \AA}$. In the morning and afternoon hours more short-lived narrower discrete arcs and bands of visual intensity (mainly the green line) are superimposed on the red belt (categories I and II in Table 4.2).

It should be noted that, occasionally, individual or sequences of transient intensifications also appear within the midday period (cf. Fig. 4.1b and event 11 in Table 4.1). Hence, the term 'midday gap' (cf. Cogger et al. 1977), frequently used to express the general low intensity of the green line near midday, is not absolute, but of statistical nature. As an atypical event, case 11 of Table 4.1 is not included in category II of Table 4.2.

The events listed in Table 4.1 are selected according to certain criteria such as stable position and distinct form. These are requirements set by the triangulation technique (cf. Sect. 2.2). In consequence, the selected forms are more intense than the average intensity of dayside auroras. Thus, the emission altitudes given in Tables 4.1 and 4.2 are generally somewhat lower than the altitude of the most common dayside auroras.

4.2 Dynamics of dayside aurora in relation to solar wind variations and geomagnetic disturbances

In the following we will concentrate on coordinated observations of dayside auroras and geomagnetic disturbances. Primary emphasis is placed on the latitudinal position of auroral luminosity. These observations will be related to information on the orientation and intensity of the interplanetary magnetic field (IMF). The physical interpretation of the experimental findings is given in Chapter 6.

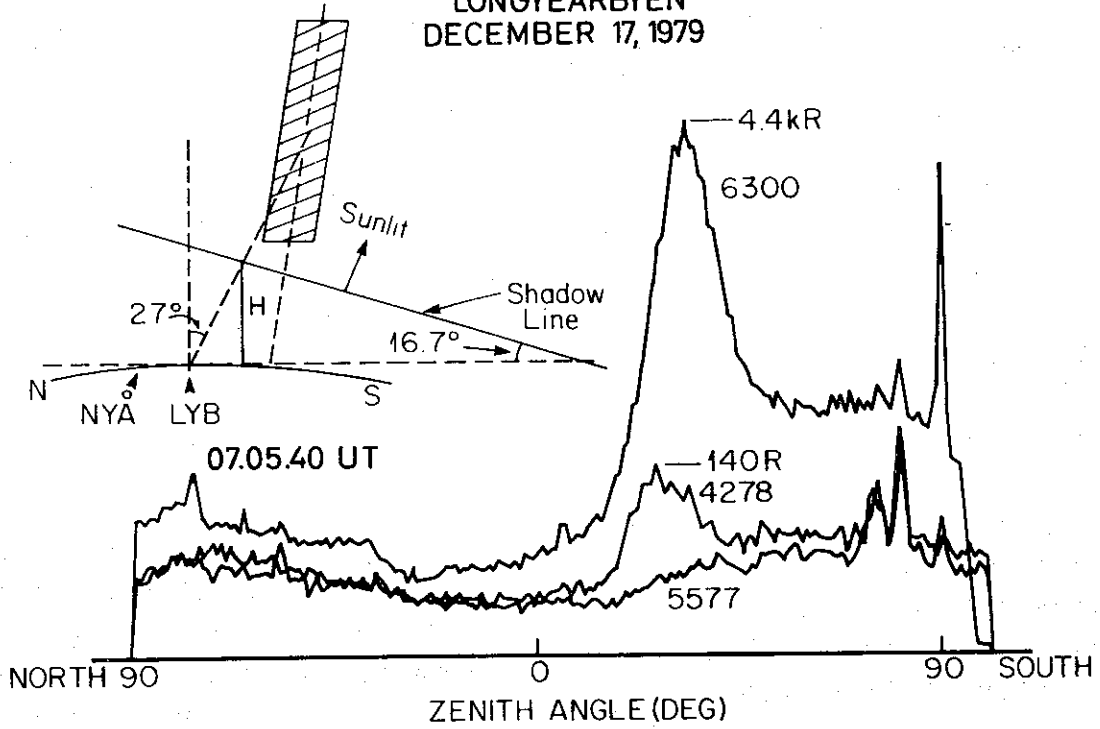
The orientation of the IMF vector is expressed in the geocentric sun-earth (GSE) coordinate system with positive X, Y, and Z-axes pointing towards the sun, the dusk side and the north, respectively. IMF variations were detected by the satellites ISEE-1 and 3 (International Sun-Earth Explorer 1 and 3). ISEE-3 was near the libration point to monitor the condition at about $250 R_E$ upstream from the earth. The position of ISEE-1 is shown in Fig. 4.2 for different auroral events which will be discussed in the following presentation. For information on the correlation between ISEE-1 and 3 IMF measurements cf. Russell et al. (1980) and Crooker et al. (1982).

December 25, 1978

On Dec. 25, 1978 similar main features of IMF variations are observed from both

MSP RECORDS
LONGYEARBYEN
DECEMBER 17, 1979

A)



LONGYEARBYEN
DECEMBER 29, 1979

B)

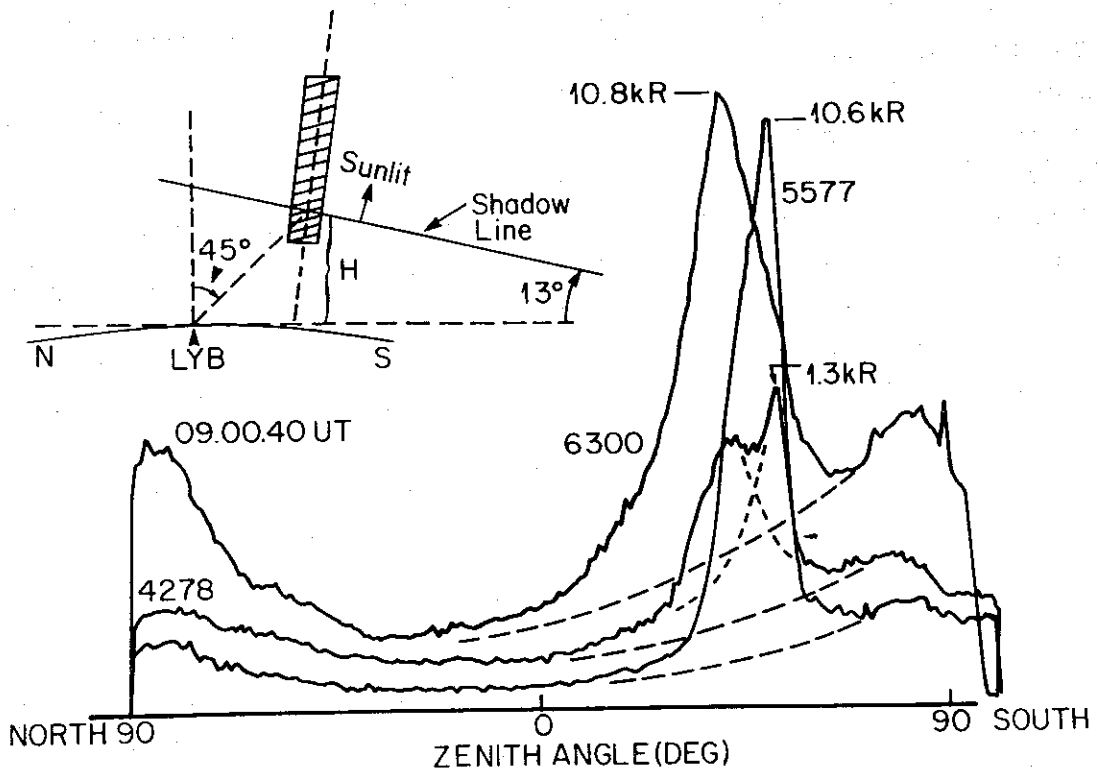


Fig. 4.1. Meridian scanning photometer (MSP) records of different, sunlit midday auroras. An illustration showing the location of parallelogram boundaries for the auroral emissions and the geometric shadow line is inserted. The time of the scan from north to south horizon was 12 sec.

spacecrafts ISEE-1 and 3. The time delay between onset at each satellite is around 1 hour. Plasmprobe data from ISEE-3 show that the solar wind speed at the spacecraft was nearly constant at ~ 370 km/s between 08 and 11 UT. At 11.20 UT, jumps occurred both in plasma speed and ion density simultaneously with a sharp B-field increase. The solar wind speed increased to ~ 420 km/s. These observations are confirmed by similar changes at ISEE-1. This indicates that the main feature of the magnetic structure is kept invariable during the expansion of the solar wind from ISEE-3 to ISEE-1. A solar wind speed of 400 km/s corresponds to a time delay between the two satellites of ~ 65 min.

Near the bowshock (ISEE-1 location) B_Z

was negative from 0730 UT. Between ~ 1030 and 1130 UT the Z-component decreased smoothly from -4γ to -7γ before the IMF again turned northward. A new southward shift started around 1220 UT. Notice the close correlation between variations of IMF B_Z , dayside auroral location and local geomagnetic activity (see Figs 4.4b and 4.5).

From Fig. 4.4A we observe sharp jumps in the B-field amplitude detected by ISEE-1 at ~ 0630 and 14 UT with no counterpart in the ISEE-3 magnetograms. In both cases the amplitude changed by a factor of three; at 0630 UT it decreased from ~ 20 to $\sim 5 \gamma$; at 14 UT B_T increased from $\sim 15 \gamma$ to $\sim 45 \gamma$. Both these shifts are accompanied by corresponding jumps in the plasma density. They are probably due to satellite-crossings

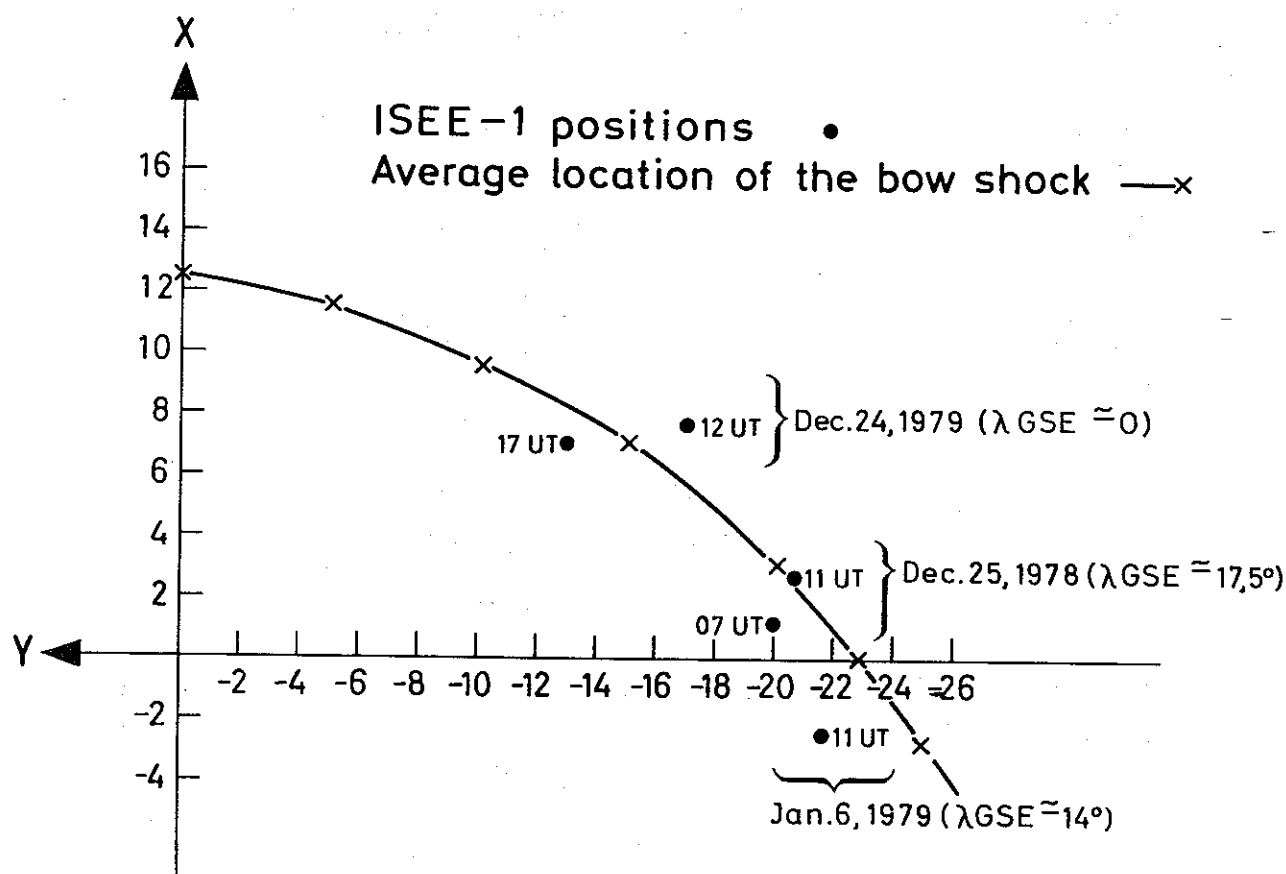


Fig. 4.2. Location of the ISEE-1 satellite at the time of different auroral events discussed in the text. The average shape of the bow shock (in GSE coordinates) is shown for a solar wind density of 10 cm^{-3} and speed $U_1 = 450$ km/s as given by the equation $0.45 X^2 + Y^2 + 1.11 Z^2 + 0.18 XY + 46.6 X - 4.16 Y - 618 = 0$ (from Formisano 1981). The latitude of the satellite position ($\lambda_{GSE} = \text{tg}^{-1}\{Z/(X^2 + Y^2)^{1/2}\}$) is given in parentheses.

TABLE 4.3

List of Geomagnetic Observatories

Station Name	Station Code	Geographic		Geomagnetic		Computed mag. dip angle	L-Value	UT of Magnetic midday (12 MLT)
		Lat.	Long. (east)	Lat.	Long.			
<u>Norway-Kola chain</u>								
Ny-Ålesund	NYA	79.00	12.00	75.44	131.45	81.5	16.5	08.30
Longyearbyen	LYR	78.20	15.70	74.36	130.94		14.4	08.30
Hornsund	HSD	77.0	15.6	73.54	127.8	81.3	13.1	08.30
Bjørnøya	BJA	74.50	19.20	71.08	124.55	79.6	9.5	08.40
Tromsø	TRO	69.20	19.00	67.14	116.80	77.6	6.3	09.10
Loparskaya	LOP	68.25	33.08	63.47	125.78	77.5	5.3	09.30
Apatity	APY	67.55	33.30	62.80	125.28	77.2	5.0	09.20
<u>Alaska Chain</u>								
Sachs Harbor	SHH	72.00	234.70	(75.96)	(28.82)			10.29
Cape Parry	CPY	70.20	235.30	(74.37)	(263.37)			10.11
Inuvik	INK	68.35	226.20	70.41	264.63	81.2	9.32	10.38
<u>Arctic</u>								
Village	AVI	68.13	214.43					11.28
Fort Yukon	FYU	66.57	214.75	66.63	256.84	78.2	6.41	11.19
College	COL	64.9	212.2	64.6	256.5	76.6	5.4	11.23
Talkeetna	TLK	62.30	209.90	61.88	257.00	74.5	4.39	11.25
<u>Alberta</u>								
<u>Fort</u>								
Providence	PROV			67.5	292.0			09.08 UT
<u>Uranium</u>								
City	URAN	59.50	251.40	67.4	304.3	81.8	7.25	08.18
Hay River	HAYR			67.3	294.3			08.58
Ft. Smith	SMIT			67.3	300.0			08.36
Ft. Chipewayan	FTCH			66.3	302.1			08.27
Ft. McMurray	FCMU			64.2	303.5			08.22
Leduc	LEDU			60.6	302.9			08.24
<u>Great Whale</u>								
River	GWR	55.28	282.17	66.54	347.29	81.00	6.93	05.00
Tixie Bay	TIXIE	71.60	128.90	60.45	191.35	82.9	5.64	15.50
Dixon Island	DIXON	73.50	80.40	62.98	161.40	83.6	6.95	16.30
Godhavn	GH	69.3	306.5	79.9	32.6	81.6	20.62	02.26
Churchill	CHUR	58.80	265.8	68.69	322.6	83.4	8.59	06.40

of the bow-shock. At the bow-shock the solar wind is compressed so that the plasma density and the magnetic field intensity is higher on the downstream side of the discontinuity. Thus, the 0630 UT transition is consistent with an outbound pass of the satellite. The satellite is estimated to be near the apogee of the orbit at 14 UT.

As observed from the geomagnetic rec-

ords in Fig. 4.5, a significant substorm occurred on the nightside with a maximum disturbance around 09 UT. A distinct auroral breakup was seen at 0847 UT on all sky camera film from the Alaskan sector. The maximum of the H-component deflection at Inuvik was more than 500 γ . Signatures of the substorm are also seen from the Canadian array of stations (midnight sector)

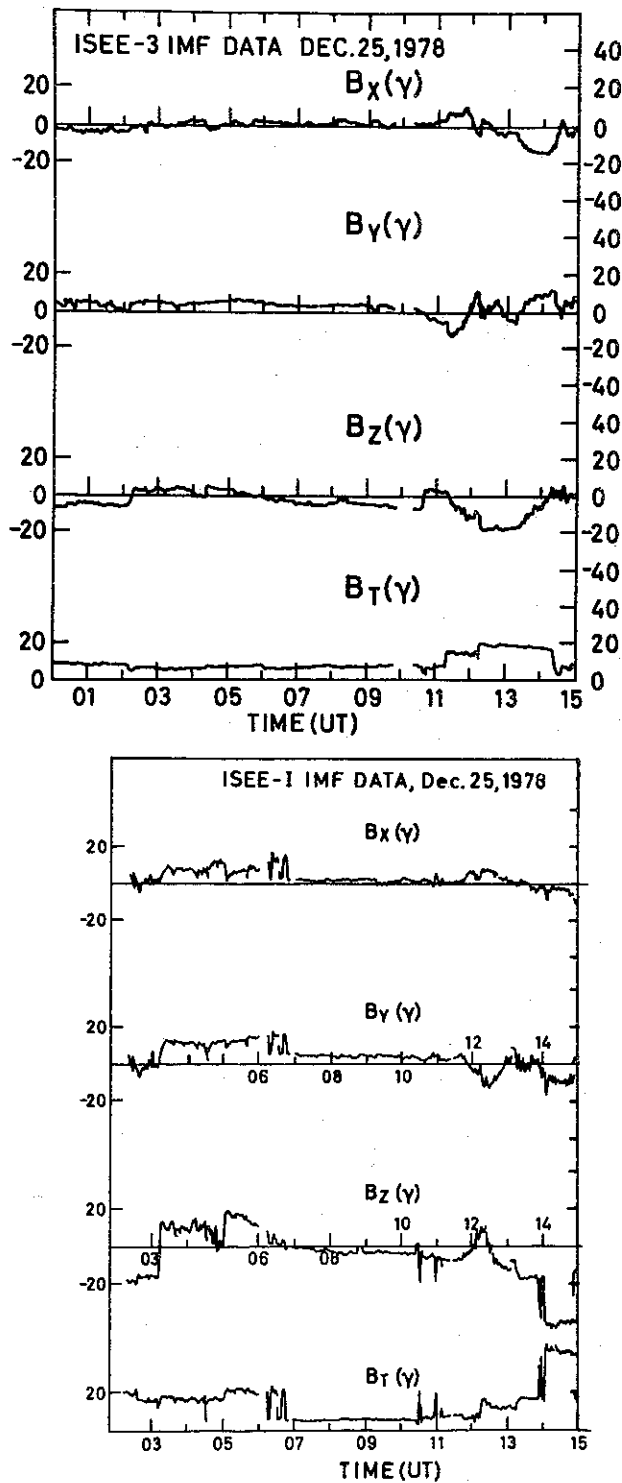


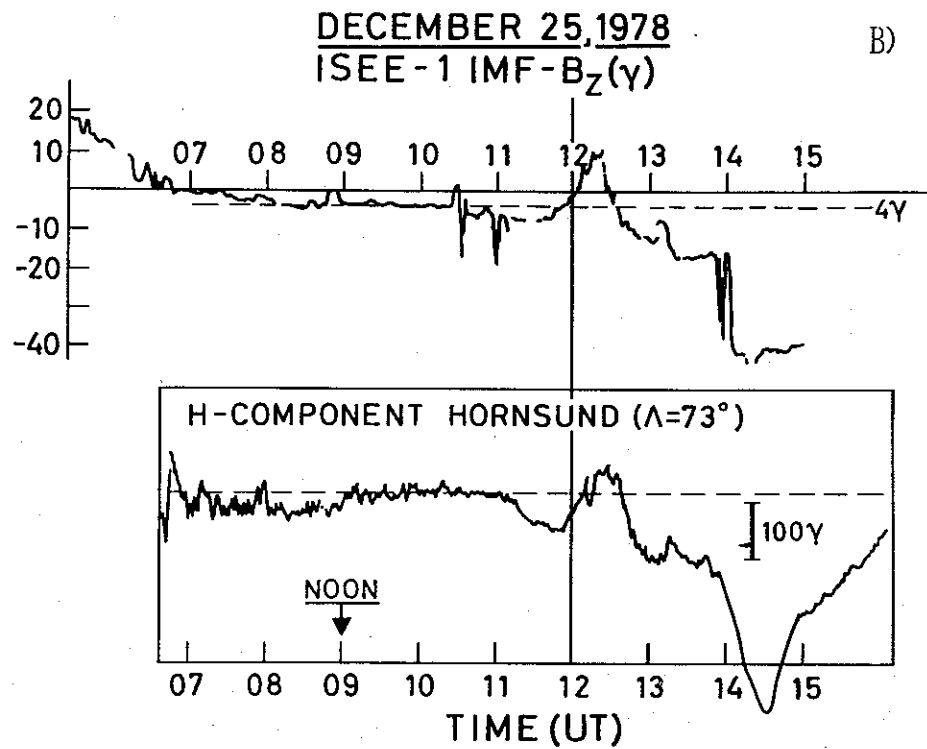
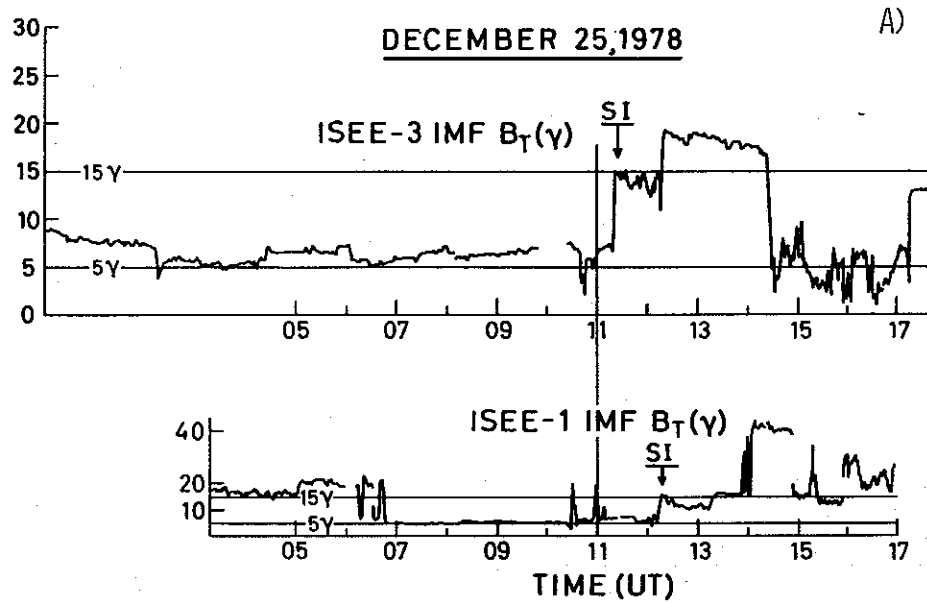
Fig. 4.3. Interplanetary/magnetosheath magnetic fields as observed from the satellites ISEE 1 and 3 for Dec. 25, 1978. The field components are shown in the geocentric sun-earth (ecliptic) (GSE) coordinate system.

and at Godhavn, Greenland; at that time in the dawn sector of the polar cap.

From Svalbard we observed a character-

istic quiet midday period from 0750 to 09 UT with auroral luminosity moving slowly southward towards the zenith of Longyearbyen. At 0902 UT discrete auroral forms appeared (Fig. 4.6). From 09 to 11 UT a sequence of discrete arcs was observed in a rather stable position near zenith. The steady, slow equatorward movement of about 1.5° (lat.) of the cusp aurora between 08 and 09 UT, as well as a slow change in the H-component, may be more closely related to a smooth southward turning of the IMF vector between 0730 and 0830 UT (Fig. 4.4B) rather than the isolated substorm on the nightside. However, the nightside activity sometimes correlates with the dayside motion, as may be seen from the Alberta array or the Alaskan chain of stations, where a maximum of the magnetic disturbance field of 370γ at ~ 1150 UT was observed at College. The corresponding local magnetic disturbance on the dayside amounted to 70γ at Hornsund station (HSD), near the poleward edge of the belt of luminosity. As can be seen from the photometer traces in Fig. 4.6 and from the all sky camera pictures in Fig. 4.7 an enhanced equatorward shift of the auroral arc started around 11 UT associated with the growth of the magnetic disturbance field. The position of maximum auroral intensity moved from 74° at 1100 UT to $\sim 71^\circ$ geom. lat. at 1140 UT.

From 1210 to 1235 the dayside aurora moved poleward at the time of decreasing disturbance field at many stations around the oval. These auroral and geomagnetic variations followed distinct changes of the direction of the IMF vector as reported above. The movement towards southeast of the IMF vector after 1220 UT (ISEE-1) was followed by a new equatorward expansion of auroral luminosity and another increase of magnetic activity. From 1315 UT the aurora was completely beyond the southern horizon at



(c)

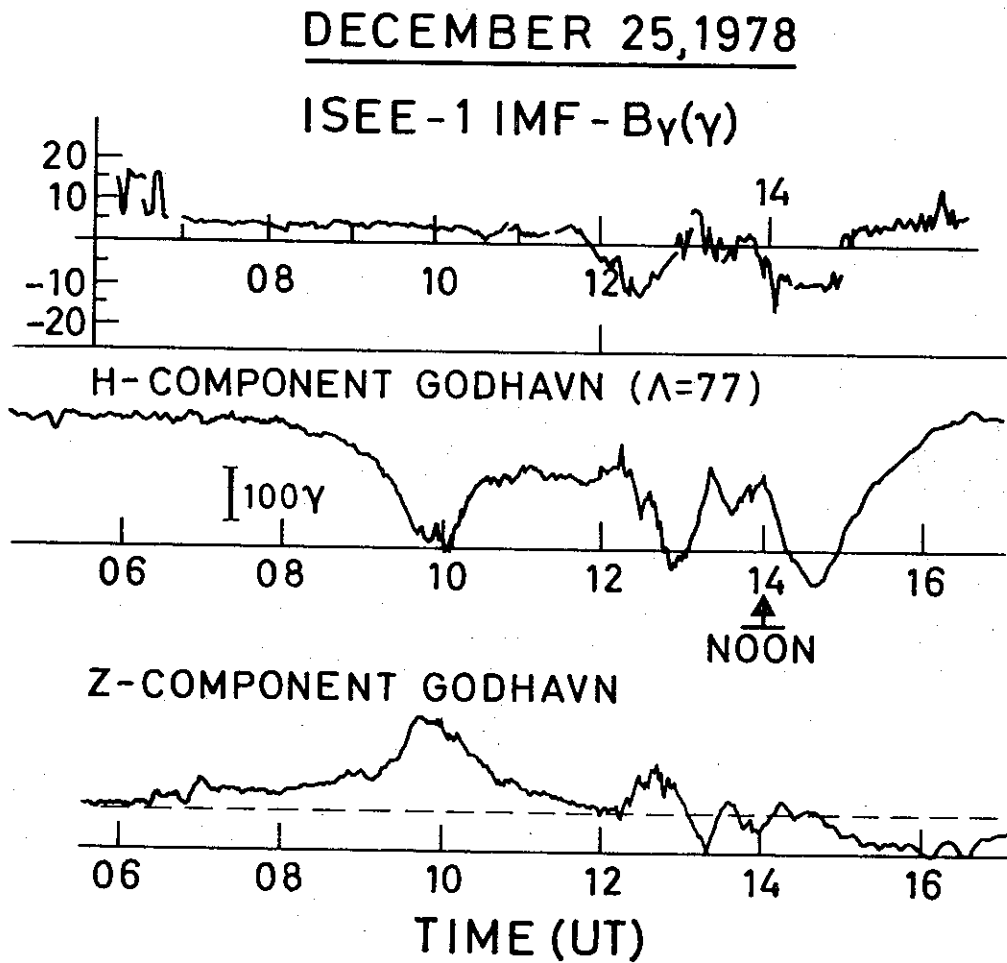


Fig. 4.4. (a) Showing the total magnetic field as detected by the two satellites ISEE 1 and 3. (b) Showing correlated variations of ISEE-1 IMF B_Z component and the horizontal component of the geomagnetic field at Hornsund, when Hornsund was to the north of the main auroral form in the post-noon sector (see Fig. 4.5). (c) Showing correlated variations of ISEE-1 IMF B_Y component and the horizontal and vertical components of the geomagnetic field at Godhavn, when Godhavn was in the noon sector of the polar cap.

GEOMAGNETIC H-COMPONENT RECORDS/DAYSIDE AURORAL LOCATION
DEC. 25, 1978

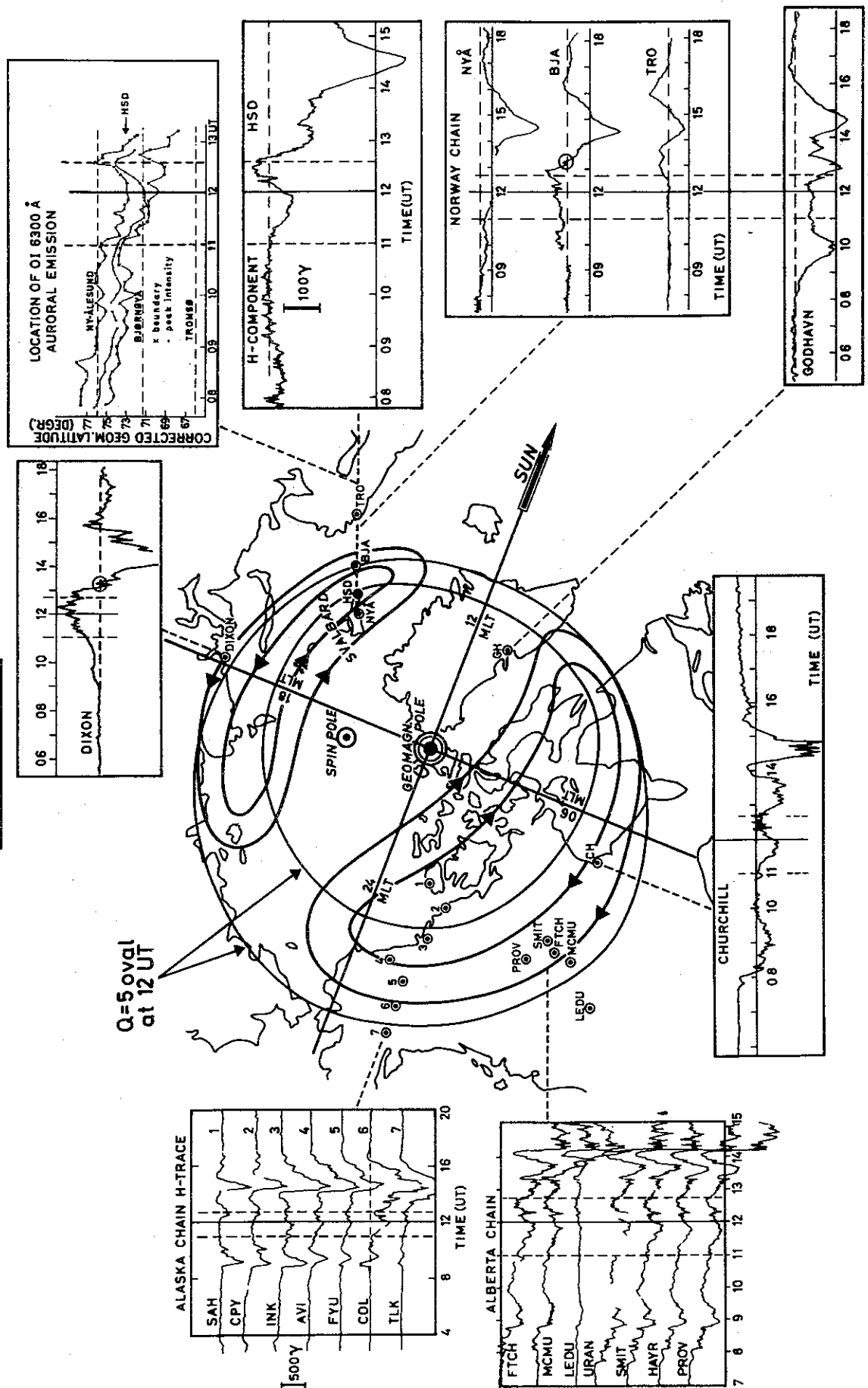


Fig. 4.5. Overview of geomagnetic and auroral post-noon sector conditions for a moderately disturbed period on Dec. 25, 1978. The latitude position of auroral luminosity at 6300 Å is shown by the solid curves in the upper right panel. Vertical lines in the magnetograms illustrate the global simultaneity of geomagnetic activity and the time relationships to the auroral latitude shifts. The crescent-shaped curves are drawn to illustrate a proposed equivalent current system for 12 UT. The statistical $Q = 5$ auroral oval is shown for 12 UT.

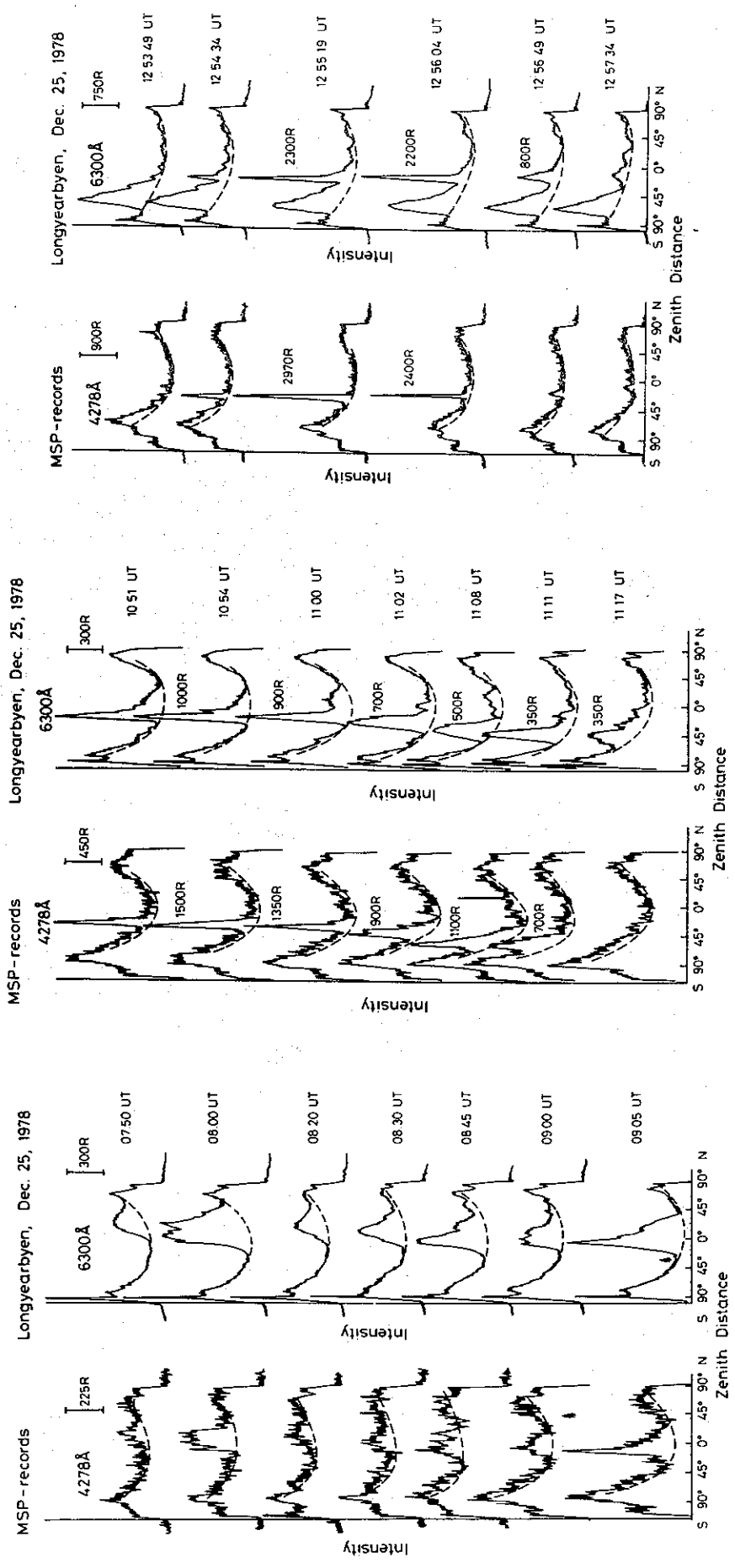
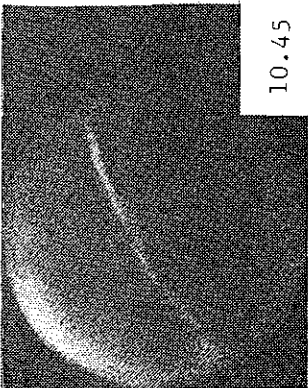
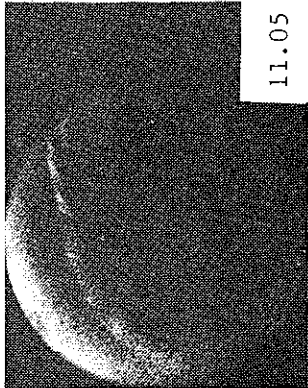


Fig. 4.6. Longyearbyen MSP records for Dec. 25, 1978. The two wavelength channels are 4278 Å N₂ ING (to the left) and 6300 Å OI (to the right). Background intensity including scattered light and airglow is indicated by the dashed curves.

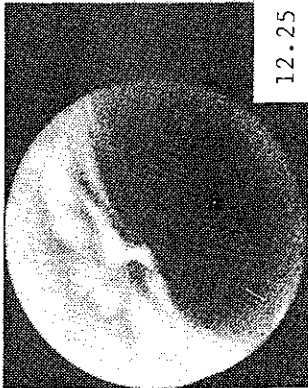
S



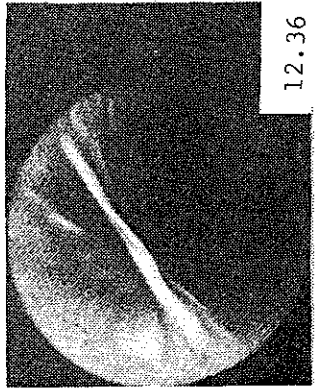
10.45



11.05

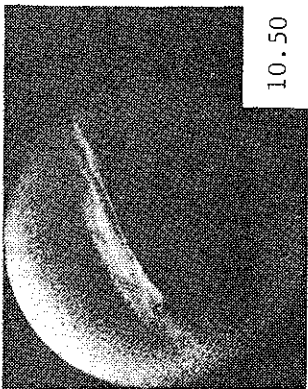


12.25

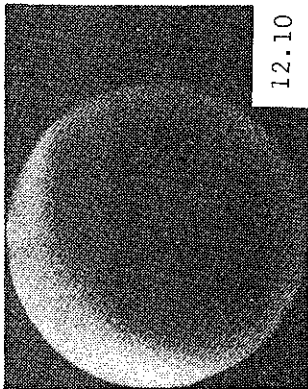


12.36

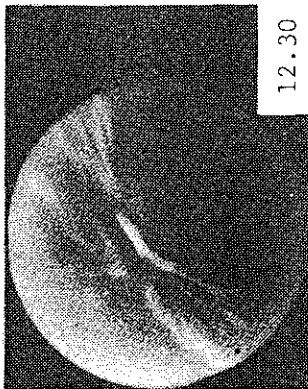
W



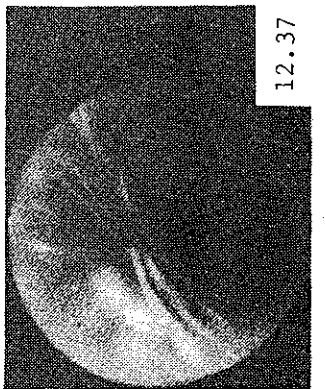
10.50



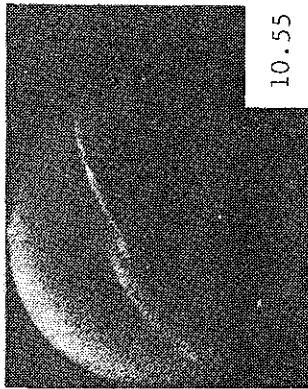
12.10



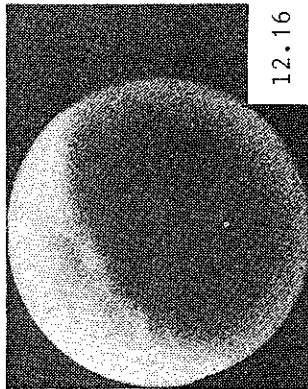
12.30



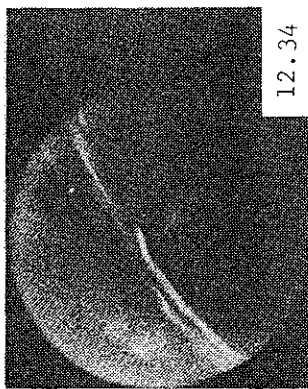
12.37



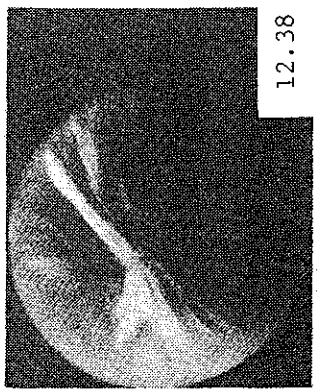
10.55



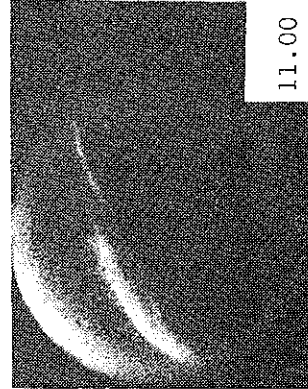
12.16



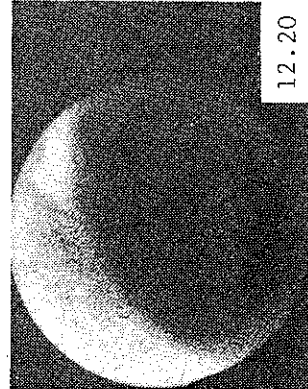
12.34



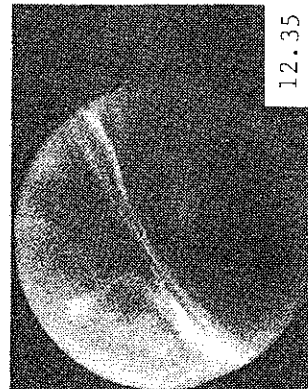
12.38



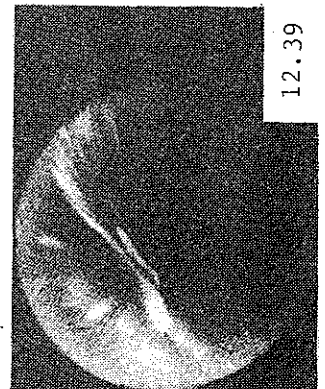
11.00



12.20



12.35



12.39

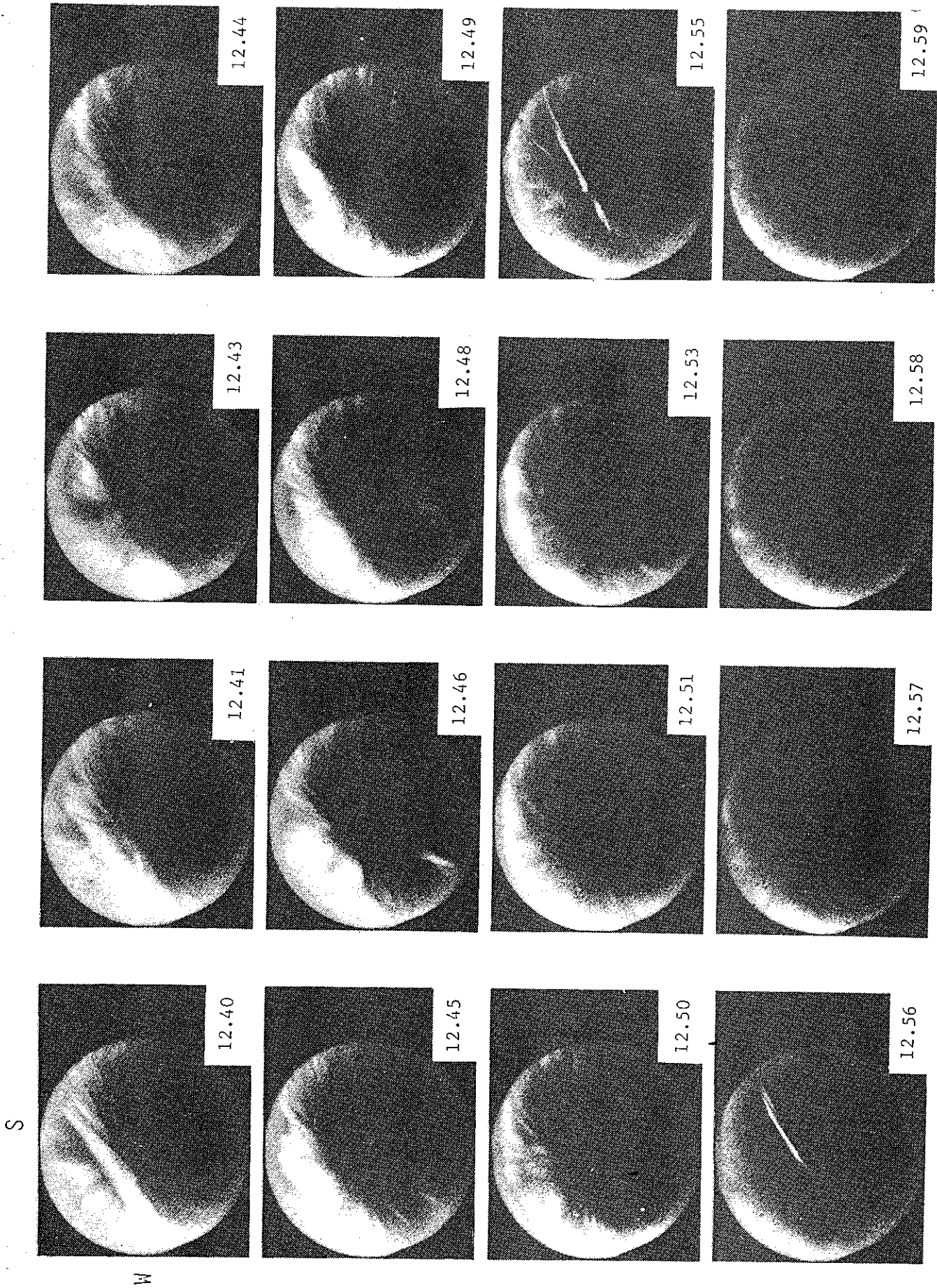


Fig. 4.7. Longyearbyen all-sky camera pictures of dayside auroral forms for Dec. 25, 1978. South is towards the top, west to the left. The time of the recordings in UT is shown to the right of each picture.

Longyearbyen. Between ~ 1330 and 1530 UT a strong red aurora was observed from Loparskaya, USSR (geom. lat. 63.5°) (Fedorova, 1982).

We notice that, during the poleward shift of the aurora, ΔH at Hornsund changed from negative to positive value when it passed the latitude of the station. When the aurora returned to lower latitudes, ΔH shifted back to negative value. The H-component deflections at Hornsund were -70γ and -130γ at 1150 and 1310 UT. The corresponding values of the IMF Z-component were -7γ and -13γ at 1130 and 1300 UT, respectively. The correlations between IMF B_z variations and latitude shifts of auroral location and H-component deflections at Hornsund are illustrated in Figs 4.4B and 4.5. A similar good correlation is observed between variations of the east-west component of IMF (B_y) and H-component variations at the polar cap station Godhaven, when Godhaven is near the noon meridian (12–16 UT) (cf. Fig. 4.4C). Local magnetic noon at Godhaven is at 14 UT.

The crescent-shaped curves in Fig. 4.5 are deduced on the basis of the magnetograms to illustrate the main feature of the equivalent overhead current system at 12 UT. Lack of data in the central polar cap prevents more detailed analysis in this region.

January 15, 1979

The main event occurred between 10 and 14 UT. An overview of the geomagnetic conditions for this event is presented in Fig. 4.8. The Kp index was 4^+ and 3^- , respectively, during the periods 09–12 and 12–15 UT. In Fig. 4.8 the time interval 10–11 UT is marked by vertical lines in the magnetograms. The period is characterized by a smooth enhancement of the geomagnetic disturbance field, coherent on global scale. Magnetograms from the auroral zone, in the late evening

to morning sector, show a negative trend in the H-component. A similar signature, although weaker, occurs at high latitudes in the early post-noon sector (Ny Ålesund-Hornsund, Svalbard), but at lower latitudes significant perturbations were not observed. In the evening sector of the auroral zone the H-component variations were positive, corresponding to an eastward equivalent current. During this period a subvisual, broad arc-like auroral form, dominated by the red oxygen line at 6300 \AA , moved equatorward from 75 to 71 degr. geom. latitude (see lower right panel of Fig. 4.8).

ISEE-3 IMF data were available from 0940 UT. From 0940 to 1030 UT B_z was between -8.5 and -6.5γ . A steady northward movement occurred between 1030 and 1120 UT; B_z was positive from 1100 UT. Assuming the magnetic structure to prevail during the expansion of the solar wind from ISEE-3 to the earth (the solar wind speed measured by ISEE-3 was 365 km/s) the time delay should be ~ 75 min. ISEE-1 (within the magnetosheat in the dawn sector) measured a steady B_z decrease from $+8 \gamma$ to -4γ between 10 and 11 UT. From 1120 to 1250 UT B_z (ISEE-1) fluctuated around zero.

The level of geomagnetic disturbance steadily increased until ~ 12 UT. Between 12 and 14 UT the activity recovered to the pre-disturbance level. The aurora, observed from Svalbard, was beyond or near the southern horizon until the start of the recovery of geomagnetic activity. Then it returned poleward (Fig. 4.8). We notice an impulsive intensification of the geomagnetic perturbation in the midnight sector at 11 UT, covering the latitude range from 65 to 71 degrees. At auroral zone latitudes in the post-noon sector an increasing positive disturbance ($\Delta H > 0$) occurred from ~ 12 UT. From that time a reversal exists in the H-

GEOMAGNETIC H-COMPONENT RECORDS/AURORAL LOCATION
JAN. 15, 1979

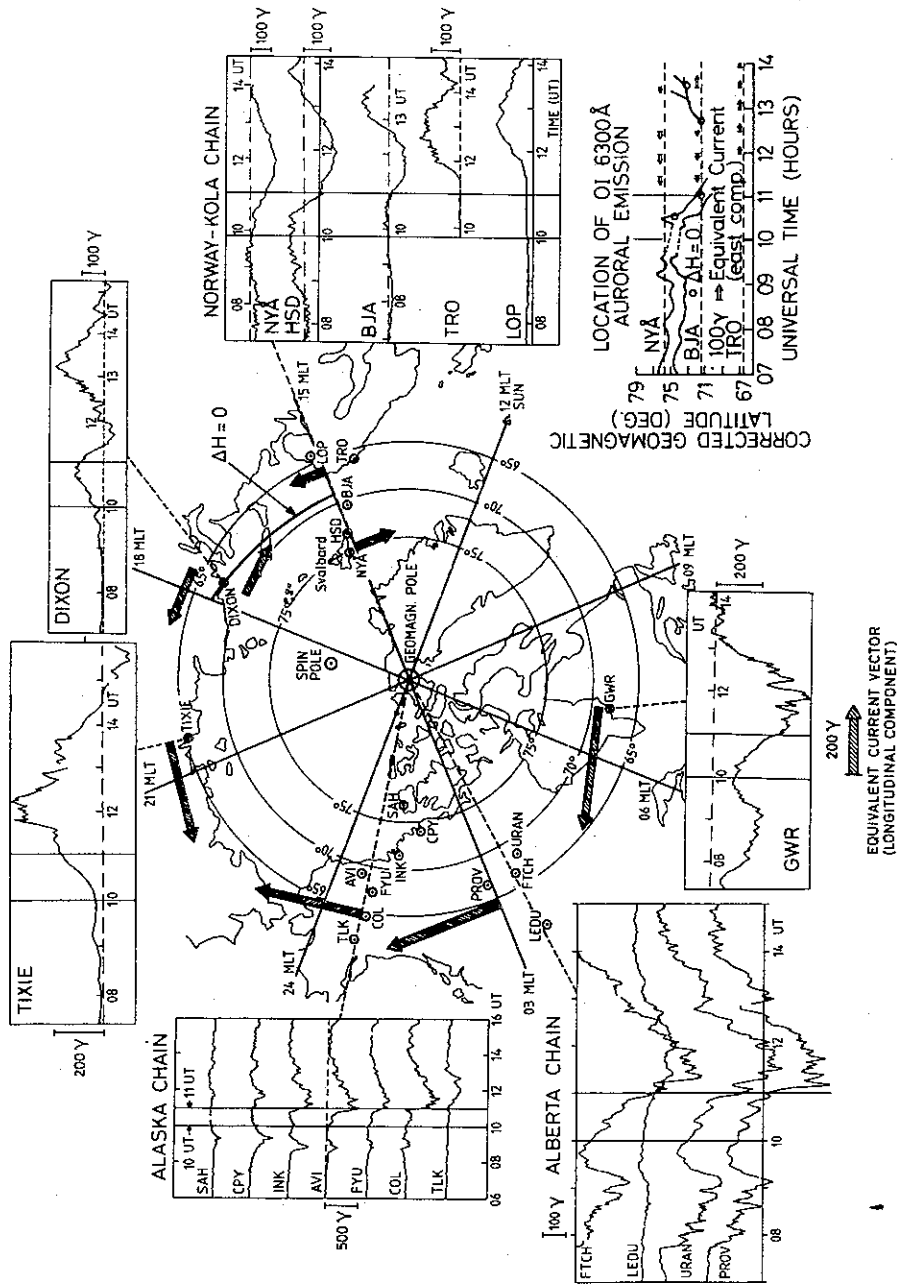


Fig. 4.8. Global-scale overview of geomagnetic conditions and location of red-dominated aurora in the post-noon sector as observed from Svalbard on Jan. 15, 1979. The coordinates of the frame of reference are corrected geomagnetic latitude and magnetic local time (MLT) (at 12 UT). The solid curves in the lower panel to the right mark the poleward and equatorward boundaries of the aurora versus local time as identified from meridian scanning photometer (6300 Å) records. Three meridian chains of H-component magnetic records are shown, one in Alaska, one in Canada, and one in Norway-Kola. Additional magnetograms from the auroral zone stations Great Whale River (GWR), Canada as well as from Dixon Island and Tixie Bay, USSR, are given. Horizontal dashed lines in the magnetograms represent the quiet-day level. From H- and Z-component records along the Norway chain and from Dixon Island the position of the geomagnetic reversal ($\Delta H = 0$) is estimated. The zonal component of equivalent current vectors at the latitude of estimated maximum intensity is marked by arrows for 12 UT.

component disturbance recorded along the Norway-Kola meridian chain of stations. This reversal ($\Delta H = 0$) in the post-noon sector coincides fairly well with the poleward edge of the main belt of auroral luminosity. It moves in latitude with the aurora—equatorward and poleward at the time of growth and decay of geomagnetic activity. A relationship between auroral shift and the local geomagnetic disturbance is illustrated by this event. When the aurora had moved to the south of Bjørnøya (BJA), after 11 UT, a negative H-component appeared in the local magnetogram (BJA) (Fig. 4.9). During the poleward return of auroral luminosity, a transition from negative to positive H-component deflection occurred at Bjørnøya when the arc passed over the station (at 12.45 UT). From 1315 UT discrete forms were seen on the photometer recordings at 6300 Å and 4278 Å ($N_2^+ 1 \text{ NG}$), moving poleward, out from the belt of more diffuse luminosity. One of these forms reached the zenith of Longyearbyen at 1345 UT, which was the instantaneous location of the geomagnetic reversal ($\Delta H = 0$, ΔZ max. negative—see Fig. 4.9).

The latitudinal variation of the H- and Z-components of the magnetic disturbance field along the Norway-Kola meridian is presented in Fig. 4.10. At the time of maximum activity (12 UT–15 MLT) H-component deflections were increasing from 40 γ at 63° to 85 γ at 67°. To the north of the peak of auroral luminosity, ΔH was negative, decreasing with latitude from -85γ at 71° to -120γ at 75°. ΔZ was zero at 67° and at 75° with negative values in between. South of 67° ΔZ was positive. It is noticed that the location of $\Delta Z = 0$ corresponds approximately to the location of maximum in H-component deflection, both in the positive and the negative regimes. A similar pattern is seen at 1245 UT ($\sim 16 \text{ MLT}$). By that time

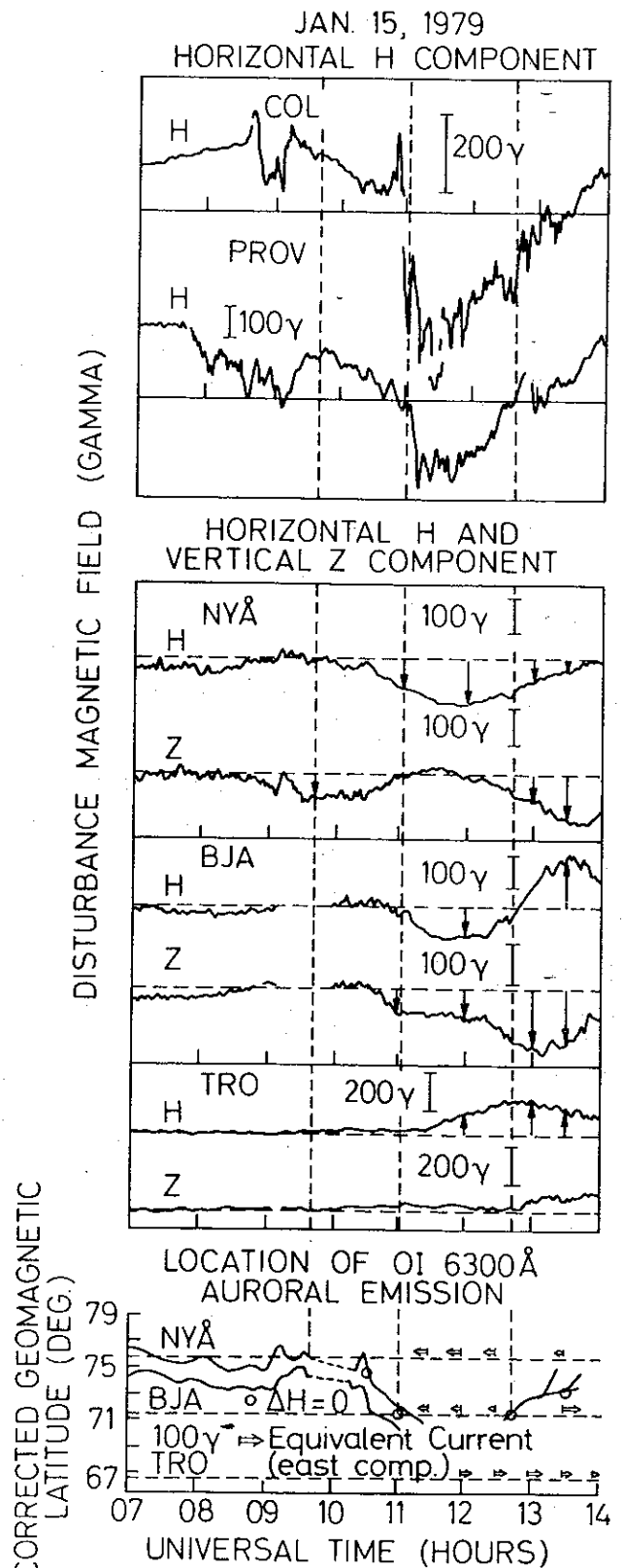


Fig. 4.9. Illustrating the latitudinal movements of day-side aurora (lower panel) in relation to night- (upper panel) and daytime (middle panel) magnetic activity.

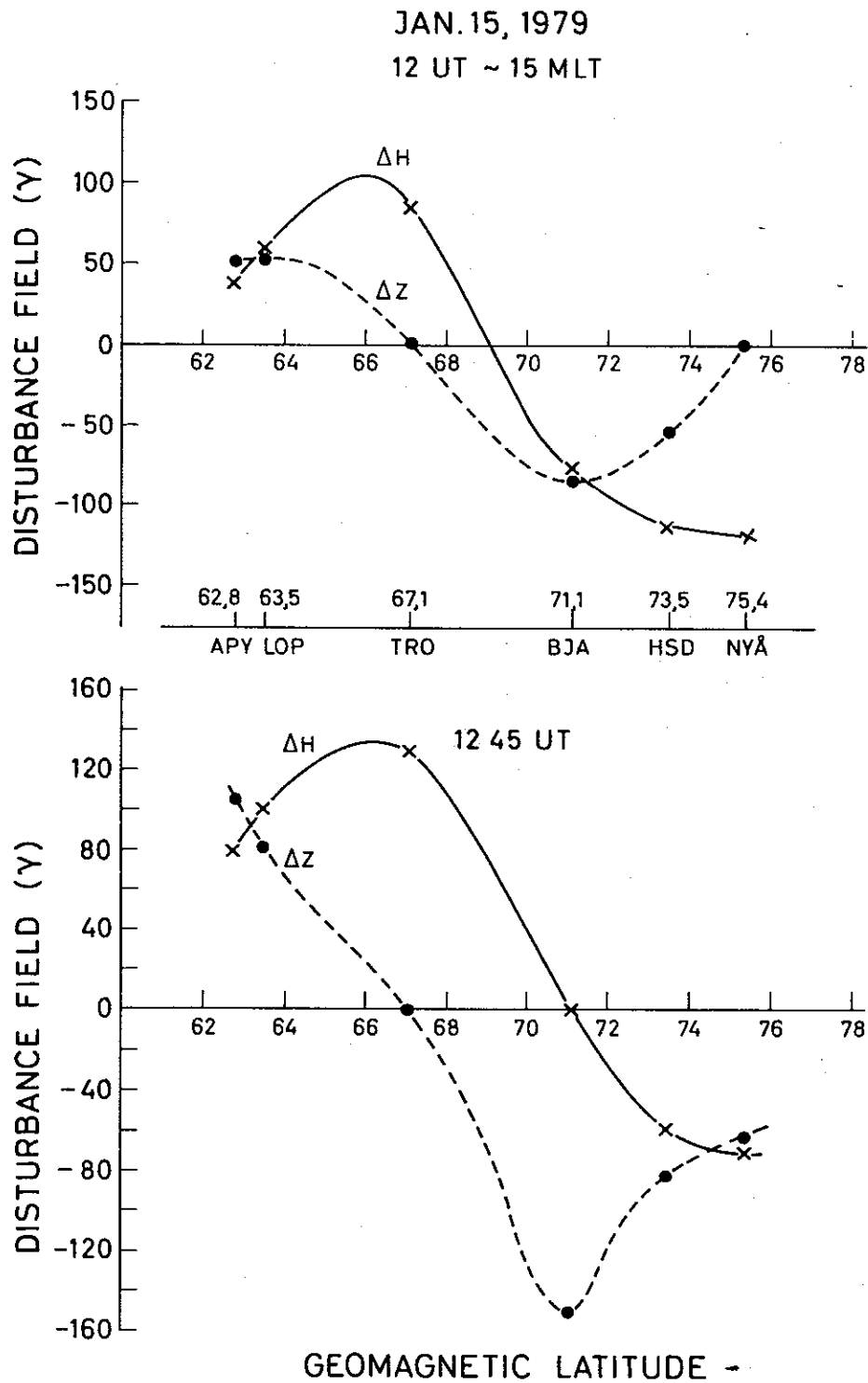


Fig. 4.10. H- and Z-component disturbance fields versus geomagnetic latitude along the Norway-Kola chain of observatories for two times during the substorm event of Jan. 15, 1979.

the transition region ($\Delta H = 0$) had shifted northward, to the latitude of Bjørnøya. The relative amplitude of deflection in the positive and negative zones had changed. Max-

imum positive ΔH had increased from $+85 \gamma$ to 130γ (66°) while peak negative ΔH had changed from -120γ to -70γ . In Figs 4.8 and 4.9 the latitude position of the $\Delta H = 0$

transition is marked for different times. It is interesting to note the coincidence of $\Delta H = 0$ transition and the poleward edge of auroral luminosity.

Figures 4.8 and 4.11 show that the amplitude variations of the H- and D-components follow each other. At the time of maximum disturbance around 12 UT, ΔD is positive

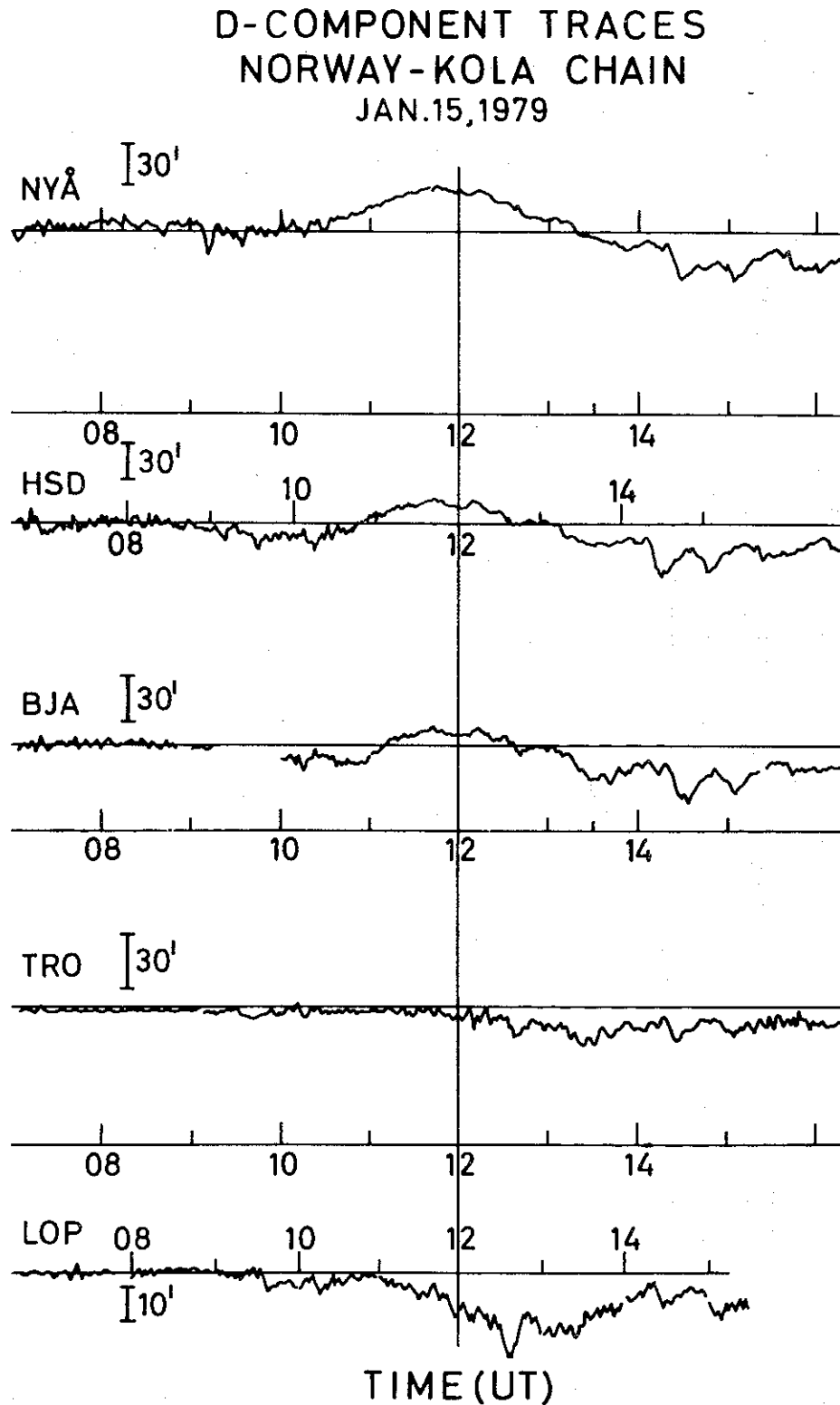


Fig. 4.11. D-component records from the Norway-Kola chain of observatories for Jan. 15, 1979. An eastward deflection is shown upward in the diagram.